River-dominated pCO$_2$ dynamics in the northern South China Sea during summer: A modeling study

Huade Zhao [a,c], Minhan Dai [a,*], Jianping Gan [b], Xiaozheng Zhao [b], Zhongming Lu [b], Linlin Liang [b], Zhiqiang Liu [b], Jianzhong Su [a], Zhimian Cao [a]

[a] *State Key Laboratory of Marine Environmental Science, College of Ocean and Earth Sciences, Xiamen University, Xiamen, China*
[b] *Department of Ocean Science & Department of Mathematics, Hong Kong University of Science and Technology, Hong Kong, China*
[c] *National Marine Environmental Monitoring Center, Dalian, China*

ARTICLE INFO

ABSTRACT

River-dominated ocean margins (RiOMars), characterized by river plumes and abundant riverine nutrient inputs, are especially critical in determining the oceanic uptake of atmospheric CO$_2$. Using a well validated three-dimensional, coupled physical-biogeochemical model, we examined the dynamics of the carbonate system in the Pearl River Plume (PRP) during summer over a typical RiOMar in the northern South China Sea (NSCS). Sea surface pCO$_2$ in the PRP was mainly influenced by a combination of physical processes, air-sea exchange, and biological activity. The interplay between these complex processes differed spatially and temporally depending on the evolution of the PRP. The latter was divided into three sub-regions: near-, mid- and far-field. In the near-field PRP, the evolution of surface pCO$_2$ was primarily influenced by biological activity. Surface pCO$_2$ decreased substantially at the initial stage as a result of phytoplankton blooms, and then increased due to the reduction in the phytoplankton and increase of zooplankton and detritus. In the mid-field, surface pCO$_2$ was initially dominated by air-sea exchange. Subsequently, the rates of biological processes exceeded the rate of air-sea exchange, resulting in a strong drawdown of surface pCO$_2$ or a strong sink for atmospheric CO$_2$. The far-field of the PRP acted as a weak CO$_2$ sink, where surface pCO$_2$ was dominated by air-sea exchange as biological processes were fairly weak. In addition, given that the air-sea CO$_2$ equilibrium time is much longer than water residence time of the PRP, the biologically-mediated low pCO$_2$ surface water was enabled to be transported far away from estuary. Taken together, the combined effect of enhanced primary production, strong plume current and strong seawater carbonate buffering capacity were responsible for maintaining low surface pCO$_2$ levels in this subtropical RiOMar system.

1. Introduction

The ocean plays an important role in mitigating the rising atmospheric carbon dioxide (CO$_2$) caused by human activities. Although it accounts for only a small surface area, the coastal ocean takes up CO$_2$ from the atmosphere at a rate of 0.19 to 0.45 Pg C yr^{-1} (Borges et al., 2005; Cai, 2011; Chen and Borges, 2009; Dai et al., 2013; Laruelle et al., 2014), which is ~40% more intense greater than that of the open ocean (Laruelle et al., 2014).

It is well known that River-dominated Ocean Margins (RiOMar) are generally key coastal systems in terms of their uptake of atmospheric CO$_2$ (Dagg et al., 2004; Guo et al., 2015; Huang et al., 2015; Ibánhez et al., 2015), due primarily to the large riverine nutrient inputs

associated with river plumes that fuels phytoplankton primary production. The latter typically refer to the buoyant freshwater overlaying the denser seawater located outside the river mouth (Hetland, 2005; Ketchum, 1983). Owing to high nutrient concentrations and low turbidity (Bauer et al., 2013; Dagg et al., 2004; Dai et al., 2008; Huang et al., 2015; Ternon et al., 2000), large river plumes, often characterized by enhanced primary production and significant consumption of dissolved inorganic carbon (DIC), act as critical atmospheric sinks of CO$_2$ for RiOMars (Chen et al., 2012). For instance, the partial pressure of CO$_2$ (pCO$_2$) in the Amazon River plume can be as low as < 200 µatm, which is much lower than the atmospheric pCO$_2$. This CO$_2$-undersaturated plume water can travel as far as ~3000 km away from the estuary, resulting in the western tropical Atlantic operating as a large atmospheric CO$_2$ sink
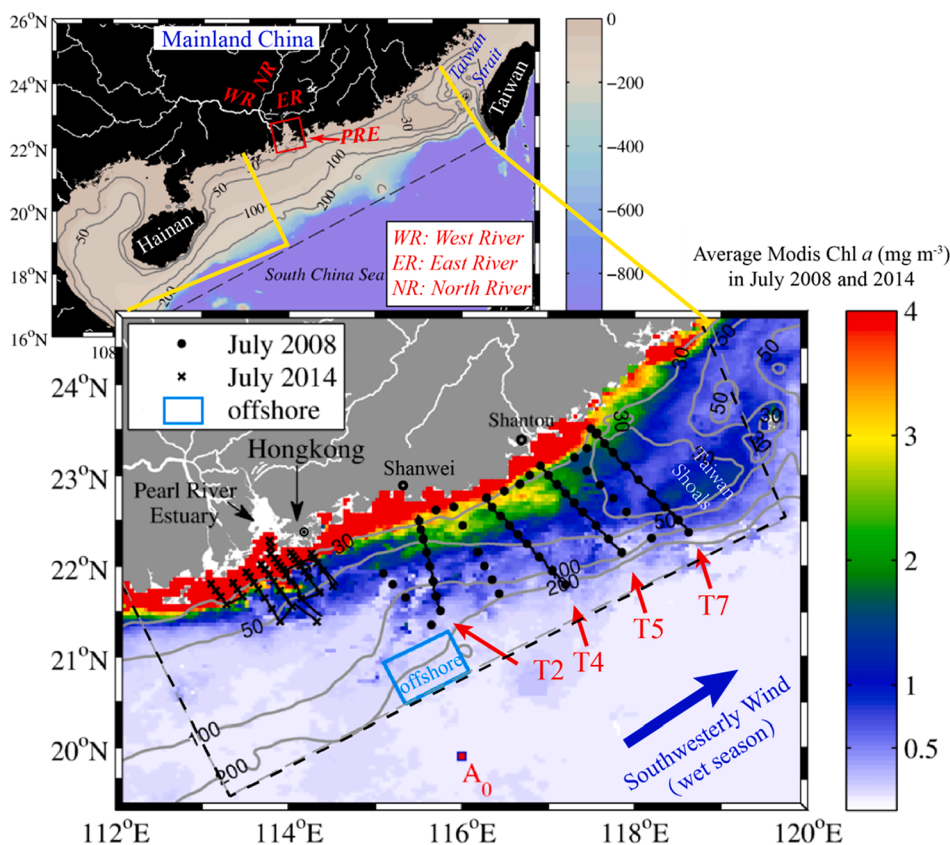
Fig. 1. Map of the northern South China Sea (a) and sampling stations during July 2008 (black circles) and July 2014 (black crosses) (b). The color contours in (b) indicates the average chlorophyll-a (Chl-a) concentration during July 2008 and 2014 based on MODIS data (http://dx.doi.org/10.5067/AQUA/MODIS_OC.2014.0). Gray solid lines indicate the isobaths. Black solid lines are cruise tracks for underway pCO_2 measurements during July 2014. T2, T4, T5 and T7 are the sections selected to compare the field observations and the simulated results. The navy blue rectangle represents the offshore region where the surface pCO_2 is slightly or not influenced by the plume and upwelled waters. The black dashed lines indicate the model domain used to compute air-sea CO_2 fluxes. "A_0" is a sampling location where its total alkalinity and dissolved inorganic carbon profiles are used for initialization of the model. (For interpretation of the references to color in this figure legend, the reader is referred to the web version of this article.)

that annually sequesters on average 7.61 ± 1.01 to 7.85 ± 1.02 Tg C (Cooley et al., 2007; Ibánhez et al., 2015, 2016; Körtzinger, 2003; Ternon et al., 2000). Elsewhere, as on the continental shelf of the East China Sea, the mean annual air-sea CO_2 fluxes reached 2.3 ± 0.4 mol C m^{-2} y^{-1}, suggesting strong uptakes from the atmosphere. The drawdown of seawater pCO_2 was significantly correlated with the Changjiang River discharge (Chou et al., 2009; Tseng et al., 2011). The importance of the river plume in modulating atmospheric CO_2 is also reflected in the fact that the East China Sea can be transformed from an atmospheric CO_2 sink to a source due to a 13% seasonal reduction of the Changjiang river discharge during summer and fall, and a 55% reduction on an annual scale (Tseng et al., 2011).

Both the Coriolis force, coastline bathymetry/geometry, the offshore pressure gradient, tidal forcing, coastal currents, and wind forcing affect the dynamics and extension of river plumes onto the shelf (Chao, 1988; Fong and Geyer, 2002; Gan et al., 2009a; Horner-Devine et al., 2015). The combination of these processes together with the varying river discharge largely modulates the temporal variation of river plumes in terms of location, structure and magnitude (Molleri et al., 2010; Walker et al., 2005). In addition to the physical dynamics, chemical and biological responses within river plumes also induce complex spatiotemporal changes (Dagg et al., 2004; Hickey et al., 2010; Dai et al., 2008; Han et al., 2012). Thus, the dynamics of pCO_2 and the air-sea CO_2 fluxes in river plumes are extremely complex as they are affected by highly variable physical and biogeochemical processes (Cao et al., 2011; de la Paz et al., 2010; Huang et al., 2015; Ibánhez et al., 2015).

Most studies reveal that the surface pCO_2 of river plumes is significantly affected by biological processes such as high primary production leading to low surface water pCO_2 (Dai et al., 2008; Huang et al., 2015). Air-sea exchange is also proposed to play an important role (Körtzinger, 2003; Zhai et al., 2009). For example, in the RiOMar system of the Pearl River estuary (PRE) and the northern South China Sea (NSCS), Dai et al. (2008) reported that surface pCO_2 in the region near and offshore of the

PRE is dominated by biological consumption. Zhai et al. (2009) further revealed that air-sea exchange greatly influences the surface pCO_2 of the Pearl River Plume (PRP) in offshore waters. However, it remains very challenging to quantify the relative importance of biological processes and air-sea exchange in modulating surface pCO_2 and their contribution in time and space. Such knowledge gaps are also prevalent in other large river plumes such as the Amazon River (Cooley et al., 2007; Ibánhez et al., 2015) and the Mississippi River plumes (Huang et al., 2015). Our understanding is limited to a large extent by the fact that it is almost impossible to quantify the impacts from the highly variable physical and biogeochemical processes in the rive plume solely based on field observations.

In this study a three-dimensional, coupled physical-biological-carbonate numerical model was developed to investigate the carbonate system dynamics of the PRP spreading over the NSCS under idealized summer conditions. The influences of biological processes and air-sea exchange on the surface pCO_2 of the PRP were compared, and other important controlling factors were also identified. Finally, a conceptual model was proposed to illustrate the spatiotemporal mechanisms controlling the surface pCO_2 in the PRP.

2. Study area

The Pearl River, which is composed of three main tributaries, the West River, the North River, and the East River, is a subtropical river with a drainage basin located south of 27 °N (Fig. 1). It ranks as the 17th largest river worldwide in terms of water discharge (283 km^3 yr^{-1}) (Dai, 2016). It is under the influence of the monsoon system, such that the discharge is high during the wet season in summer and low during the dry season in winter, with peak discharge in July. Freshwater from the Pearl River empties into the NSCS through three subestuaries, the Lingdingyang, Modaomen and Huangmaohai. The Lingdingyang subestuary, traditionally known as the PRE, contributes 50–55% of the

Pearl River freshwater discharge (Dai et al., 2014).

Freshwater discharged from the Pearl River forms a bulge in the vicinity of the PRE mouth. Forced by coastal currents, freshwater from the outer portion of the bulge flows downstream and forms a buoyant plume over the shelf, i.e., the PRP (Gan et al., 2009a). The movement of the PRP over the shelf is controlled by various factors, such as the ambient coastal current, river discharge, wind conditions, the lateral density gradient and bottom topography (Gan et al., 2009a; Ou et al., 2009). Under the influence of the typical southwesterly wind in summer, the PRP moves eastward to the east of the PRE with a direction nearly parallel to the coastline. It then veers offshore along the ~50 m isobaths when it encounters the widening isobaths located east of Shanwei. As the PRP progresses southeastward, it widens, deepens and bifurcates into two braches near the Taiwan Shoals (Fig. 1b) (Gan et al., 2009a, b).

The Pearl River delivers a considerable amount of nutrients into the NSCS shelf. The concentrations of nitrate (NO_3), phosphate (PO_4) and silicate (SiO_3) of the PRP are 10 to 100-fold higher than those found in NSCS surface water. Such high nutrients can greatly stimulate primary production (Han et al., 2012), resulting in the frequent occurrence of phytoplankton blooms in the PRP. The phytoplankton biomass of the PRP can increase several folds during blooms, and net community production can reach up to 70–110 mmol C m^{-2} d^{-1} (Dai et al., 2008). Consequently, primary production during blooms causes a substantial uptake of CO_2 in the PRP with surface pCO_2 levels as low as ~200 μatm, i.e., half of those typical of NSCS surface water (Dai et al., 2008; Zhai et al., 2009). Thus, under the influence of the PRP, the NSCS behaves as an atmospheric CO_2 sink during summer, in contrast to other regions of the South China Sea (Zhai et al., 2013).

3. Methods

3.1. Model setup and implementation

3.1.1. The physical module

The Regional Ocean Model System (ROMS) was used to model three-dimensional, time-dependent, oceanographic flows governed by hydrostatic primitive equations (Shchepetkin and McWilliams, 2005). This physical model has been successfully used to demonstrate the evolution of the PRP off the PRE (Gan et al., 2009a) and shelf circulation over the widened shelf of the NSCS, and to determine the forcing mechanisms involved (Gan et al., 2009b). The model domain extended from 15.99°N, 108.17°E in the southwest corner to about 25.81°N, 119.54°E in the northeast corner with its central axis directed 23° anticlockwise from true east (Fig. 1). A curvilinear grid with a (450,140) dimensional array was adopted for the horizontal coordinates (x, y), forming on average a 3 km horizontal grid size. The stretched, generalized, terrain-following, s-coordinate (Song and Haidvogel, 1994) was applied for the vertical coordinates, with control parameters $\theta_s = 2.5$ and $\theta_b = 0.8$ to increase the vertical resolution in surface and bottom boundary layers. The model had 30 vertical levels with a minimum grid spacing of < 1 m in the nearshore water column and ca. 10 m over the outer shelf. A local closure scheme, based on level-2.5 turbulent kinetic energy equations (Mellor and Yamada, 1982), was adopted in the vertical mixing parameterization. The water depth was obtained by merging ETOPO2 (1/30°) from the National Geophysical Data Center (USA) and by digitizing depths from navigation charts published by China's Maritime Safety Administration. The minimum water depth was set equal to 5 m, and the topography was smoothed slightly to reduce truncation errors.

The physical module, which was forced by the open boundary conditions (Gan and Allen, 2005), was initialized with horizontally uniform temperature and salinity profiles, and the initial velocities and surface elevations were set to zero. Spatially uniform southwesterly wind stress (0.025 Pa) and a constant discharge rate of 16,500 m^3 s^{-1} were applied to stimulate typical summer conditions of the NSCS. The salinity, temperature and NO_3 concentration of the water column at the head of the PRE were set to 10, 29.5 °C and 60 mmol m^{-3}, respectively. More details

about the settings and results of the physical model are presented in Gan et al. (2009a, b).

3.1.2. The biological module

The biological model was based on the widely applied Fasham model (Fasham et al., 1990) embedded in ROMS (Fennel et al., 2006; Hofmann et al., 2008). This NPZD ecosystem model, including components of nitrogen, phytoplankton, zooplankton and detritus, has successfully simulated the nutrient dynamics and the ecosystem evolution in the PRP (Gan et al., 2010). The major processes involved are as follow (Fig. S1): the NO_3 and ammonium (NH_4) are utilized by the phytoplankton; the latter is grazed and assimilated by zooplankton; small and large detritus are produced by the activity of phytoplankton and zooplankton, and finally detritus is decomposed to NH_4 via remineralization. The dynamic equations for different components and processes are outlined in Appendix A. A series of sensitivity tests were conducted to optimize the biological parameters (Gan et al., 2010) based on previous studies (Fennel et al., 2006; Spitz et al., 2005). Results are shown in Table D1 and as detailed in Gan et al. (2010).

Following the method used for physical variables, the biological variables were initialized with horizontally uniform values. The initial profiles were obtained from field observations of NO_3 and chlorophyll-*a* (Chl-*a*), and were generated from a one-dimensional model after a 1 year run. Details of the processing methods are presented in Gan et al. (2010).

3.1.3. The carbonate system module

The carbonate system model embedded in ROMS was adapted by Fennel et al. (2008) from Zeebe and Wolf-Gladrow (2001), with total alkalinity (TA) and DIC as model tracers (Fig. S1). The former is modulated by physical processes, nitrification and new production, and the latter is determined by physical processes, air-sea exchange and biological processes including primary production, remineralization and zooplankton metabolism. Seawater pCO_2 in the surface layer, calculated from DIC, TA, temperature and salinity according to CO2SYS (Lewis and Wallace, 1998), was used to quantify the air-sea CO_2 exchange. Details of the governing equations are described in Appendix B.

As in the biological module, the initial DIC and TA on the shelf of NSCS were horizontally identical based on observations at a deep water station (A_0 in Fig. 1) conducted on the R/V Dongfanghong II during August 2009. The concentrations of DIC and TA at the head of the PRE were calculated based on their conservative mixing lines during July (Guo et al., 2008). To match a salinity of 10 in the physical and biological modules, the corresponding conservative concentrations of DIC and TA were 1644 and 1774 μmol kg^{-1}, respectively. The atmospheric pCO_2 was set to 370 μatm based on field observations.

3.1.4. Model implementation

Based on the configurations described in Sections 3.1.1–3.1.3, a standard model was used to simulate the dynamics of the carbonate system in the NSCS under typical summer conditions. Additionally, a control run was implemented based on the standard model by turning off the biological processes and air-sea exchange to create a baseline of biogeochemical variables that were solely determined by mixing processes. Both the standard and control runs were processing for 40 days, and the daily-averaged results were used for the analyses.

3.2. Observational data

Observation data from two cruises were used to validate the model. One was carried out from 30 June to 12 July 2008 (R/V Shiyan III), mainly covering the shelf of the NSCS, and the other was conducted during July 2014 (R/V Kediao 8) when the vicinity of the PRE was surveyed (Fig. 1). The occurrence of obvious blooms was revealed by satellite-derived Chl-*a* during both cruises (Fig. 1). The distribution of high Chl-*a* concentrations agrees well with the pathway of the PRP, showing a jet-like, high Chl-*a* belt extending from the PRE to ~117°E,
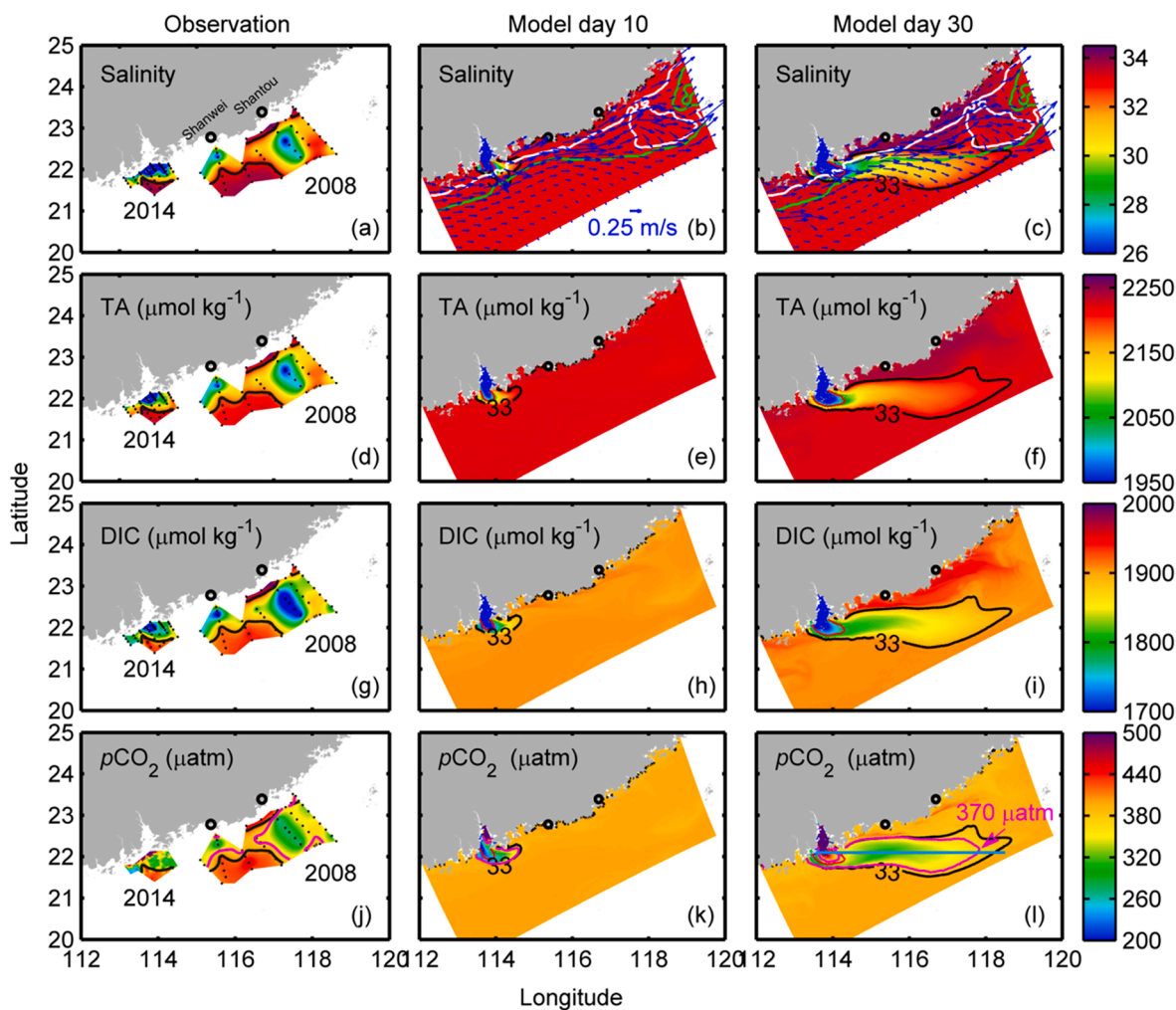
Fig. 2. Surface salinity (a, b, c), TA (d, e, f), DIC (g, h, i) and pCO$_2$ (j, k, l) during field observation (left), model results on day 10 (middle) and day 30 (right). Red and black solid lines indicate the 25 and 33 salinity contours, respectively. White and green solid lines in panels (b) and (c) indicate the 30 and 50 m isobaths, respectively. Blue arrows in (b) and (c) indicate surface currents. Magenta solid lines in panels (j), (k) and (l) indicate the 370 μatm pCO$_2$ contours. The blue solid line in panel (l) indicates the transect along 22.1°N used to demonstrate the dynamics of the carbonate system in the Pearl River Plume and its controlling mechanisms. Observed salinity, TA and DIC in 2008 are modified from Cao et al. (2011), and observed salinity and DIC in 2014 are modified from Su et al. (2017). Observed pCO$_2$ in 2008 is calculated using CO2SYS (Lewis and Wallace, 1998) based on the observed DIC and TA, while observed pCO$_2$ in 2014 was measured using the underway pCO$_2$ system. (For interpretation of the references to color in this figure legend, the reader is referred to the web version of this article.)

roughly along the 50 m isobaths. The sampling stations well covered this high Chl-a region.

Measurements and distributions of temperature, salinity, DIC and TA in 2008 were reported in Cao et al. (2011), and those of temperature, salinity and DIC in 2014 were published by Su et al. (2017). Briefly, seawater temperature and salinity were measured onboard with a Sea-bird Conductivity-Temperature-Depth (CTD) unit and an SBE-19-plus/SBE-25 profilers in July 2008 and July 2014, respectively. Discrete samples for TA and DIC analysis were collected with Niskin bottles attached to a Rosette sampler. Both TA and DIC samples were poisoned with HgCl$_2$-saturated solution, 100 μL for TA and 50 μL for DIC. The TA and DIC samples were stored in 100 mL polyethylene bottles and 40 mL borosilicate glass vials, respectively. The TA was determined by Gran acidimetric titration of a 25 mL sample. The DIC was measured by acidification of 0.5–0.7 mL of a water sample and then the concentration of CO$_2$ was quantified with a nondispersive infrared detector (Li-7000 NDIR). Both methods have a precision of $\pm$ 2 μmol kg^{-1} with calibration by certified reference material from the Scripps Institution of Ocean-ography, CA, USA. The atmospheric and surface water pCO$_2$ during July 2014 were determined using an underway system equipped with a continuous flow and cylinder-type equilibrator. The water sample was

continuously pumped into the equilibrator where the CO$_2$ equilibrated between the water and headspace gas. Subsequently, the latter was dehydrated, and the CO$_2$ molar fraction in the dry air was detected using a Li-7000 NDIR spectrometer with calibration by CO$_2$ gas standards (Dai et al., 2008; Zhai et al., 2009).

4. Results and validations

4.1. Results

4.1.1. Surface distribution

As previously reported (Cao et al., 2011; Gan et al., 2010), three types of water masses can be identified in the surface layer of the NSCS under typical summer conditions: PRP water, upwelled water and the typical NSCS offshore surface water. The PRP water is defined as the water masses with salinity 0 to 33 (Gan et al., 2009a; 2010), and the upwelled water refers to upwelled bottom and subsurface water with salinity > 33.75 (Gan et al., 2010).

Based on the modeled surface salinity and current (Fig. 2), fresh-water from the Pearl River is constrained at the mouth of the PRE, forming a bulging feature during the first 10 days. Then the plume
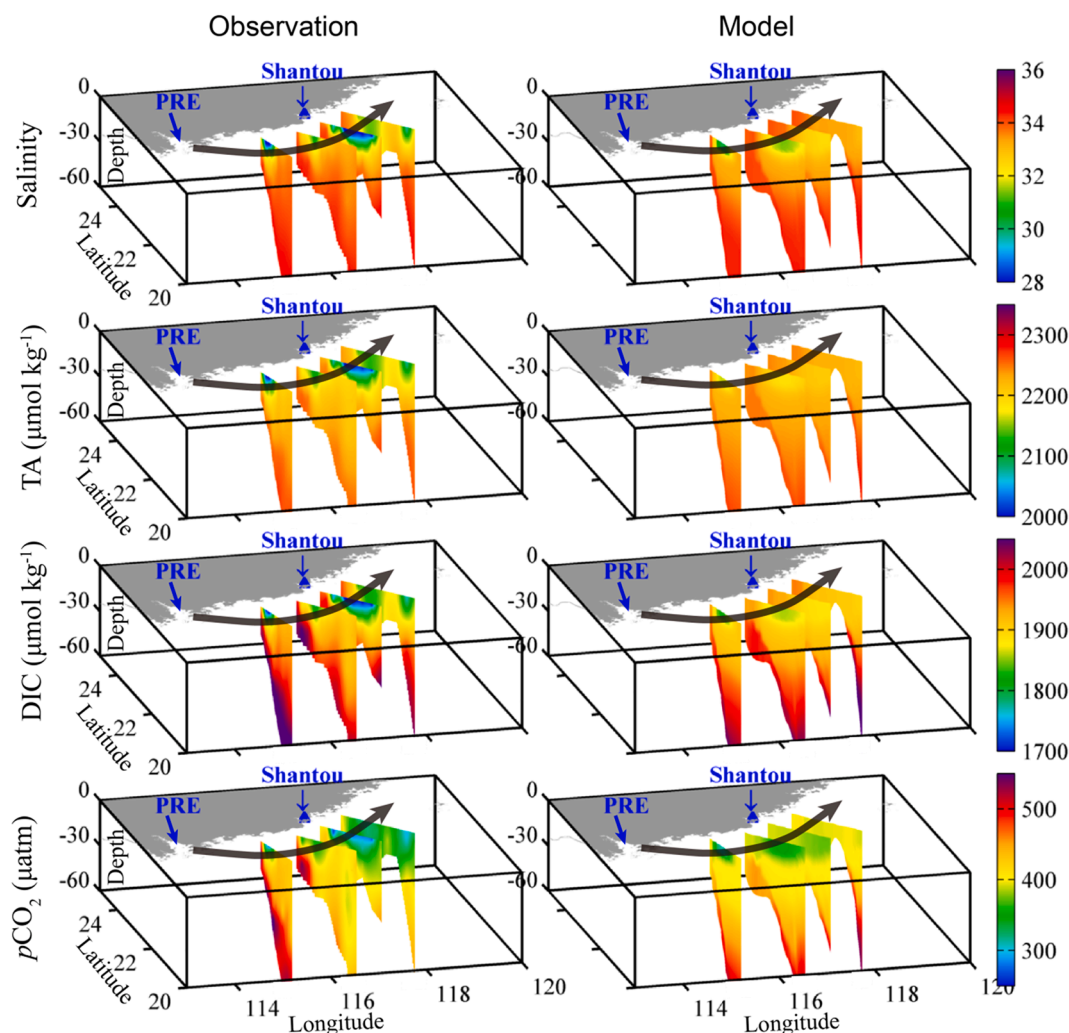
Fig. 3. Comparison between observations and results of model simulations in the vertical distribution of salinity, TA, DIC and pCO_2 at transects T2, T4, T5 and T7 (localities are shown in Fig. 1). Model results were obtained on day 30, i.e., during the mature stage of evolution of the Pearl River Plume. Grey arrows indicate the direction of spreading of the plume water.

water, driven by coastal currents, was delivered eastwardly roughly following the 50 m isobaths along a latitude of 22.1°N, and subsequently bifurcated into two branches near the Taiwan shoals on day 30 as previously reported by Gan et al. (2009a, b). Overall, the model in the present study was able to adequately simulate the spreading of the plume over the shelf of the NSCS as revealed by the observed surface salinity (Fig. 2). Here, the PRP travels eastwardly from the PRE to the shelf of the NSCS roughly along the 50 m isobaths. Under typical summer conditions when southwesterly wind prevails, intensified upwelling is formed and eventually outcropped at the lee of a coastal cape, e.g., Shantou and Shanwei (Fig. 2) caused by intensified upslope advection of dense deep waters (Gan et al., 2009b). The wind-driven upwelling considerably modulates the dynamic of the PRP. In turn, the upwelling circulation is largely shaped by movement of the PRP (Gan et al., 2009a).

The dynamic of NO_3, phytoplankton, zooplankton and Chl-*a* in the NSCS during summer are also well simulated by our model (Gan et al., 2010). The extensions of NO_3 are much shorter alongshore and offshore than those of the salinity in the PRP. Moreover, NO_3 is nearly undetectable in the surface layer and increases gradually as depth increases. The PRP behaves as a biological active region in term of the Chl-*a* concentrations derived from the satellite data, field measurements and model results. The phytoplankton growth and zooplankton biomass are higher in the plume region than in the typical NSCS water.

The distributions of the modeled TA and DIC in the surface layer were correlated well with those of salinity over time (Fig. 2): the simulated TA and DIC of the PRP were clearly lower than those of the offshore surface water, while the highest TA and DIC appeared in the nearshore close to Shantou where the high salinity subsurface water upwelled (Fig. 2). The surface TA was 2149 ± 115, 2224 ± 4 and 2243 ± 4 µmol kg^{-1} in the PRP (S $\leq$ 33), offshore water ($33 < S < 33.75$) and upwelled water (S $\geq$ 33.75), respectively. The corresponding surface DIC was 1837 ± 73, 1908 ± 5 and 1940 ± 9 µmol kg^{-1}, respectively. The observed DIC and TA were also positively correlated with salinity (Fig. 2). The averaged surface TA increased from 2108 ± 76 µmol kg^{-1} in the PRP to 2205 ± 7 µmol kg^{-1} in the offshore water, and increased to 2235 ± 12 µmol kg^{-1} in upwelled water. The averaged surface DIC was 1813 ± 74, 1916 ± 12 and 1962 ± 23 µmol kg^{-1} in the PRP, offshore water and upwelled water, respectively. Both the modeled and observed TA and DIC displayed an increasing trend from the PRP to offshore water to upwelled water.

The modeled pCO_2 exhibited large variations between difference regions (Fig. 2). It decreased markedly from $>$ 500 µatm in the inner estuary to 355 ± 71 µatm in the PRP, and then increased to 397 ± 5 and 393 ± 8 µatm in offshore water and upwelled water, respectively. The distribution of observed pCO_2 demonstrated the same pattern with that of the modeled results (Fig. 2). During July 2008, the observed pCO_2 in the PRP was 342 ± 40 µatm, and was much lower than surface pCO_2 in
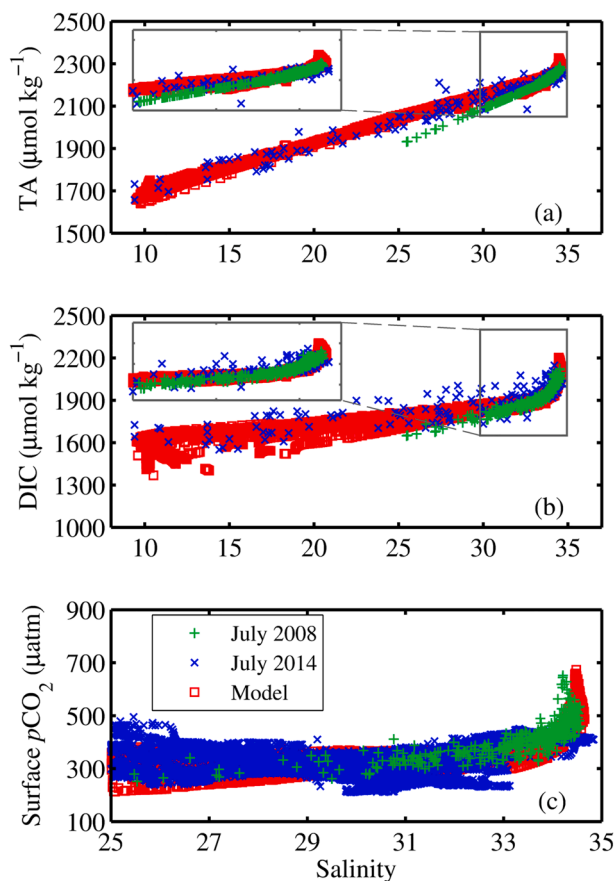
Fig. 4. Relationships between salinity and carbonate parameters compared between model simulations (day 30) and observations: (a) TA, (b) DIC and (c) surface pCO_2.

the offshore water and upwelled water, i.e., 417 ± 14 µatm and 421 ± 28 µatm, respectively. During July 2014, surface pCO_2 decreased significantly from the inner estuary to the PRP, i.e., from 595 ± 227 to 304 ± 38 µatm. Both the model and observation revealed that the PRP behaved as a significant atmospheric CO_2 sink, while the offshore water and upwelled water released CO_2 to the atmosphere.

4.1.2. Vertical structures

The vertical distributions of the modeled carbonate system at transects T2, T4, T5 and T7 were derived from model outputs on day 30 (Fig. 3), when the mature stage of the PRP was attained (Gan et al., 2010). Based on the model and observation results (Fig. 3), the vertical salinity distributions between the model and observations yielded a similar PRP pathway during summer, i.e., delivered seaward and eastward away from the PRE. In addition, the highly saline subsurface water climbed shoreward and upwelled from the nearshore region. The vertical distributions of the modeled carbonate system were comparable with those of the observations, showing that TA, DIC and pCO_2 in subsurface water were higher than those in offshore surface water, and also higher than those in plume water (Fig. 3).

Overall, the model reasonably simulated the dynamics of the carbonate system in different water masses of the NSCS during summer. The model, however, did not reproduce the readily detected freshwater patch observed at transect T5. This inconsistency was primarily attributed to the difference in the magnitude of the river discharges between the model configuration and observations: the river discharge of the model was set at a constant of 16,500 $m^3 s^{-1}$, representing typical summer condition, whereas the observed river discharge during June and July 2008 was much higher and more variable (from ~20,000 to

~43,000 $m^3 s^{-1}$) (Cao et al., 2011).

4.2. Model validation

We have shown in a qualitative way that our model was successful in simulating the spread of the PRP and the distributions of the carbonate system in different water masses of the NSCS during summer. Given that TA and DIC in the NSCS are mainly determined by the mixing of end-members, the modeled results were further quantitatively validated based on the relationships between salinity and the core parameters of the carbonate system, i.e., TA and DIC. Modeled results within the observed depth (<200 m) on day 30 were used to compare with the observations (Fig. 4). Results showed that the observed salinity was > 25 during 2008, but spanned a broader range during 2014. Overall, the relationship between modeled salinity and TA (or DIC) agreed well with those of the observations. Based on the average TA at 0.5 salinity intervals, the mean difference between the modeled TA and the observations was 3.0% in 2008 (correlation coefficient, $r^2 = 0.99$) and 0.7% in 2014 ($r^2 = 1.00$) (Fig. S2). Following the same methods, the mean difference in the DIC between the model and observations was 2.4% in 2008 ($r^2 = 0.80$) and 1.5% in 2014 ($r^2 = 0.95$). It can thus be argued that the model performed reasonably well in simulating TA and DIC, as was also supported by the consistent seawater pCO_2 values obtained out of the Pearl River mouth between the model and observations (Fig. 4c).

The observed TA and DIC at salinities < 30 during 2008 were lower than those of the modeled results as well as the observations during 2014. These discrepancies are mainly attributed to the difference of the river discharges: the extremely high discharge during 2008 led to a remarkable dilution of TA and DIC concentrations in the freshwater end-member. Taken together, the above results indicate that the model in this study can effectively simulate the pathway of the PRP and the characteristics of the carbonate system therein, providing a high level of confidence in its capacity to investigate the dynamics of the carbonate system and the variable spatiotemporal controlling mechanisms of the PRP under summer conditions.

5. Discussion

5.1. Air-sea CO_2 fluxes

River plume plays an important role in regulating pCO_2 in RiOMars (Ternon et al., 2000; Tseng et al., 2011; Huang et al., 2015; Cao et al., 2020). To evaluate the influence of the PRP, the model domain (Domain in Fig. 5) was divided into three water masses including the PRP (PRP in Fig. 5), the upwelled water (Upwelling in Fig. 5) and the typical NSCS offshore surface water (Offshore in Fig. 5). The daily averaged surface pCO_2 and air-sea CO_2 fluxes in these different water masses were computed.

The simulated daily averaged pCO_2 in the offshore surface water was almost constant at ~400 µatm (400 ± 1 µatm), and was comparable to the observed surface pCO_2 at the offshore station A_0 (Fig. 1), whilst the surface pCO_2 in the upwelled water varied around ~390 µatm (392 ± 2 µatm). The distribution of pCO_2 in the PRP fluctuated from ~300 to 360 µatm, exhibiting an inverse relationship with the phytoplankton biomass (Fig. 17 in Gan et al. (2010)). The offshore and upwelling region degassed CO_2 to the atmosphere at rates of ~1 and 0.8 mmol C m^{-2} day^{-1}, respectively. In turn, the PRP is a strong atmospheric CO_2 sink, with an average uptake rate of 1 mmol C m^{-2} day^{-1}. The maximum rate was 2.28 mmol C m^{-2} day^{-1} on day 9.

Since averaged surface pCO_2 increased continuously in the upwelled water and was nearly constant in the offshore surface water, the decline in pCO_2 in the Domain was primarily attributed to that in the PRP. Furthermore, the averaged surface pCO_2 in the PRP increased gradually after day 9, indicating that the corresponding pCO_2 decrease in the Domain largely resulted from the spatial expansion of the PRP into the NSCS. Parallel to the increase in surface area of the PRP from 0 to ~30%
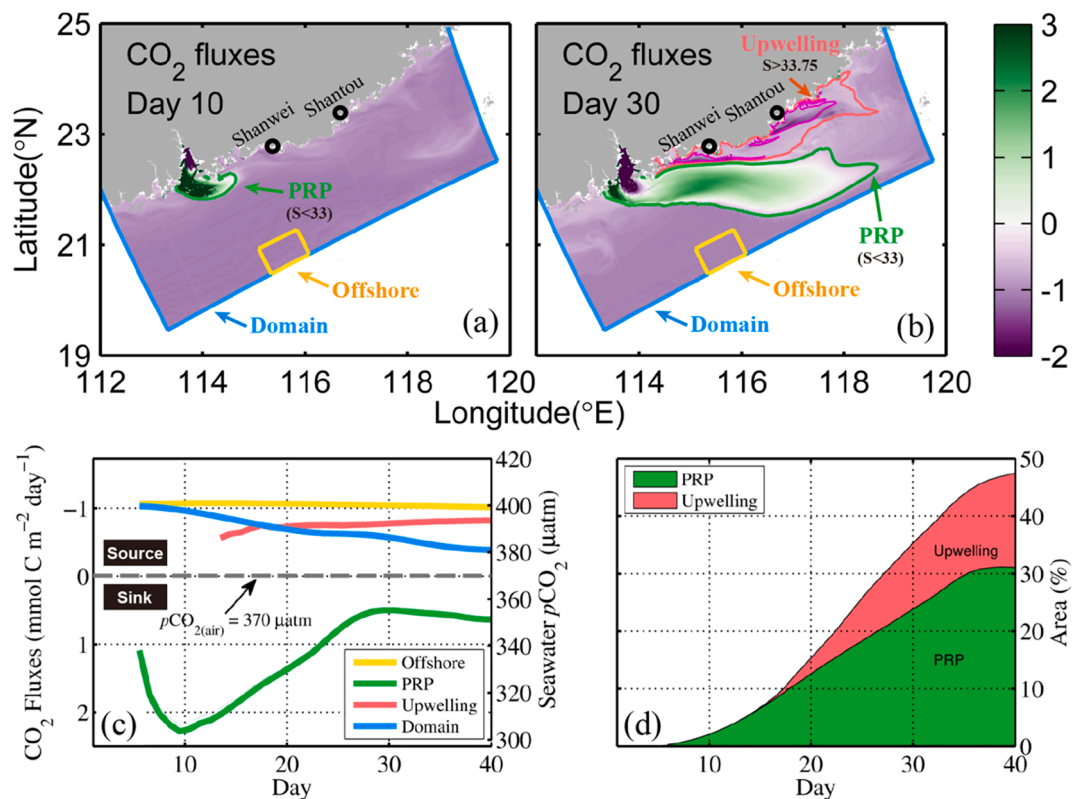
Fig. 5. Air-sea CO_2 fluxes on day 10 (a) and day 30 (b) in mmol C m^{-2} day^{-1}, time series of daily averaged air-sea CO_2 fluxes (reversed y-axis) and surface pCO_2 in different water masses under study (c), and the areal percentage of upwelling and plume coverage accounting for the modeling domain (d). Offshore, PRP, Upwelling and Domain represent the typical offshore surface water, the Pearl River Plume, the upwelled water and the model domain of the northern South China Sea, respectively. Locations of Domain and Offshore are indicated by the blue and yellow rectangle, respectively. PRP (green) and Upwelling (red) change dynamically associated with the salinity. (For interpretation of the references to color in this figure legend, the reader is referred to the web version of this article.)

(Fig. 5b), the averaged surface pCO_2 and air-sea CO_2 degassing fluxes of the Domain decreased from ~400 to 380 μatm and 1.05 to 0.37 mmol C m^{-2} day^{-1}, respectively (Fig. 5a).

In RiOMars, both the surface pCO_2 and the areal coverage of the plume are critical to air-sea CO_2 fluxes in the adjacent marginal sea (Ibánhez et al., 2016; Tseng et al., 2011). Unfortunately, the high variability of pCO_2 and the area of the river plume lead to difficulties in accurately quantifying air-sea CO_2 fluxes, resulting in exclusion of the river plumes from many estimates of global air-sea CO_2 fluxes (Bauer et al., 2013; Chen et al., 2013). Reliable quantifications of river plumes and the associated air-sea CO_2 exchange can be crucial in determining whether a continental shelf behaves as a CO_2 sink or source and estimates of the oceanic CO_2 uptake at global scale (Bauer et al., 2013).

5.2. Spatiotemporal dynamic of pCO_2 in the PRP and its controlling mechanisms

5.2.1. Dynamics of the ecosystem and carbonate systems

In this idealized model, the variation of air-sea CO_2 fluxes was mainly modulated by the dynamic of sea surface pCO_2. The daily simulated results in the surface layer at the transect along 22.1°N (Fig. 2), i.e., the principal axis of the PRP spreading on the shelf of the NSCS (Gan et al., 2009a), were used to explore the controlling mechanisms of the CO_2-uptake in the PRP. The boundary of the PRP derived from the salinity distributions is marked by the green solid lines in Figs. 6–8.

The PRP water arrived at the transect along 22.1°N on ~day 5, and then gradually spread eastward. In the PRP, the NO$_3$, DIC and pCO_2 (standard model run) were much lower than their corresponding concentrations determined by mixing processes (control model run), clearly indicating consumption for these variables (Fig. 6). In contrast, TA

behaved conservatively as evidenced by the fact that the differences in daily averaged TA between the standard and control runs were < 0.3%.

Based on the dynamics of the ecosystem and carbonate systems, the surface layer of the PRP can be characterized by three sub-regions, including the so-called near-field (<114.1°E), the mid-field (114.1°E − 115.5°E) and the far-field (>115.5°E) based on the distance away from the PRE. In the near-field region, enriched nutrients (Fig. 6b) triggered a robust phytoplankton bloom (Fig. 7a) between days 5 and 20, resulting in a primary production estimate two orders of magnitude higher than that in the offshore surface water outside the PRP (Fig. 7b). The corresponding surface pCO_2 was much lower than atmospheric CO_2, with a mean value of 277 ± 56 μatm (Fig. 6e and Table 1). After day 23, zooplankton growth suppressed that of the phytoplankton (Fig. 7). Compared with the stage of the phytoplankton bloom, the average biomass of phytoplankton decreased from 61 to 12 mmol C m^{-3}, while the zooplankton increased from 8 to 21 mmol C m^{-3}. The corresponding primary production decreased greatly, from 73 to 16 mmol C m^{-3} day^{-1} (Fig. 7b). The surface pCO_2 increased to 418 ± 79 μatm, with the maximum value of 585 μatm (Fig. 6e). In the mid-field region, the concentrations of NO$_3$ (Fig. 6), and the abundance of phytoplankton (22 mmol C m^{-3}) and zooplankton (11 mmol C m^{-3}) (Fig. 7) were moderately high compared with those in the near- and far-fields regions. The corresponding surface pCO_2 (Fig. 6e), 320 ± 23 μatm, was lower than the atmospheric pCO_2. In the far-field region, NO$_3$ concentrations and phytoplankton biomass were relatively low, comparable to those in oligotrophic NSCS surface water, and the surface pCO_2 mostly ranged from ~320 to 370 μatm, with an average value of 343 ± 18 μatm (Fig. 6e). The concentration of detritus decreased gradually from near-field (83 mmol C m^{-3}) to mid-field (49 mmol C m^{-3}) and far-field regions (36 mmol C m^{-3}) (Fig. 7d).
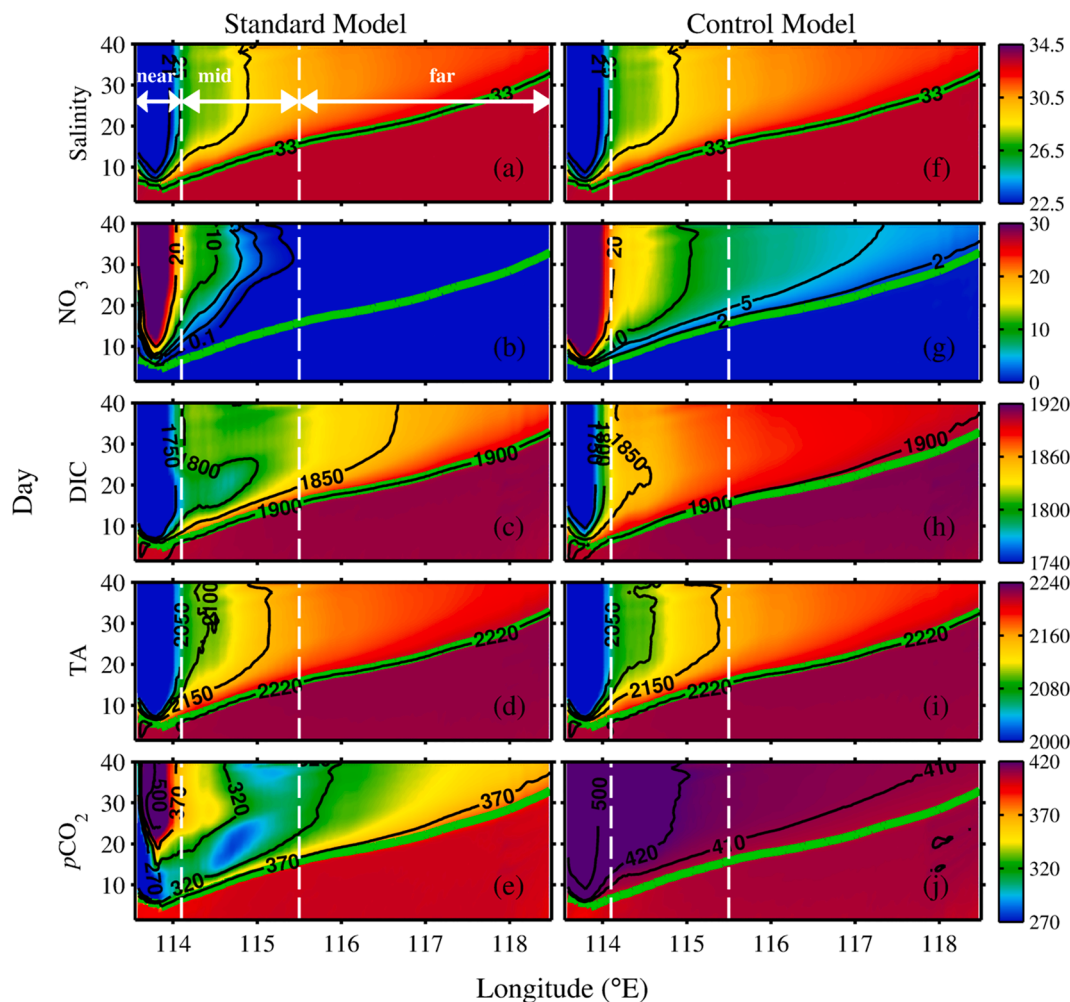
Fig. 6. Time series of along-plume surface salinity (a), nitrate, NO₃ (b), DIC (c), TA (d) in µmol kg⁻¹, and pCO₂ in µatm (e) in the surface layer as a function of longitude along the plume axis (22.1°N). Results of the standard model are shown in panels (a) to (e), and results of the control case are shown in panels (f) to (j). The green solid lines indicate the boundary of the Pearl River Plume (33 salinity contours). White dashed lines represent the boundaries of near-field, mid-field and far-field regions. (For interpretation of the references to color in this figure legend, the reader is referred to the web version of this article.)

5.2.2. Effect of biological processes on sea surface pCO₂

To quantify the effects of individual biological processes on sea surface pCO_2, we derived the corresponding DIC and TA variation, and then computed the corresponding changes in pCO_2 based on the model's governing equations (Appendix C). The evaluated biological processes included the primary production, the remineralization of detritus, and zooplankton metabolism and excretion, referred to as zooplankton activity. Noting that the mean depth of the upper mixed layer in the PRP was ~5.5 m, much shallower than the corresponding water depth of ~45 m (Zhao et al., 2017), we consider that benthic processes play a minor role in affecting surface pCO_2 in the PRP, thus the benthic DIC export from sediment was not included in this study.

Primary production primarily consumed CO_2 (Fig. 8a), whereas zooplankton activity (Fig. 8b), and remineralization (Fig. 8c) both generated CO_2. Overall, the pCO_2 consumption rate by primary production, $(\partial pCO_2/\partial t)_{Prim}$, was greater than the addition rate by remineralization and zooplankton activity, i.e., $(\partial pCO_2/\partial t)_{Remi}$ and $(\partial pCO_2/\partial t)_{Zoop}$, respectively. Thus, the summation of $(\partial pCO_2/\partial t)_{Prim}$, $(\partial pCO_2/\partial t)_{Remi}$ and $(\partial pCO_2/\partial t)_{Zoop}$, defined as the net effect of the ecosystem, was positive and primarily played a role in the drawdown of surface pCO_2 (Fig. 8d).

The surface pCO_2 consumption rate by enhanced primary production was averagely 85 ± 42 µatm pCO_2 day⁻¹ in the near-field during the phytoplankton bloom stage, which was about an order of magnitude higher than the pCO_2 addition rate by remineralization or zooplankton activity. The net ecosystem effect thus resulted in a notable drawdown of pCO_2, with the consumption rate of 83 ± 42 µatm pCO_2 day⁻¹. During the zooplankton proliferation stage in the near-field, the pCO_2 consumption rate decreased markedly owing to the reduction in phytoplankton biomass (Fig. 7a), while the pCO_2 addition rate increased and was attributed to the enhancement of zooplankton activity and detritus remineralization. Consequently, the drawdown of pCO_2 by the net ecosystem effect was low, < 20 µatm pCO_2 day⁻¹ from day ~25 to 30 (Fig. 8d). In the mid-field region, the pCO_2 consumption rate by primary production, with an average value of 29 ± 20 µatm pCO_2 day⁻¹, intensified gradually over time at any given location, generally increasing from < 5 µatm day⁻¹ to > 20 µatm day⁻¹. Zooplankton activity and detritus remineralization played minor roles in changing surface pCO_2 production rate (<3 µatm pCO_2 day⁻¹). Thus the net effect of the ecosystem was dominated by primary production, with a net consumption rate of 26 ± 19 µatm pCO_2 day⁻¹. In the far-field region, all the individual biological terms were fairly weak. For instance, pCO_2 consumption rate by primary production was 3 ± 1 µatm pCO_2 day⁻¹, which agreed well with observations (<1.5 µatm pCO_2 day⁻¹) conducted west of the far-field region (Zhai et al., 2009 in Fig. 9a). Overall, the net effect of the ecosystem was a negligible CO_2 consumption with a rate of 0.3 ± 0.6 µatm pCO_2 day⁻¹.
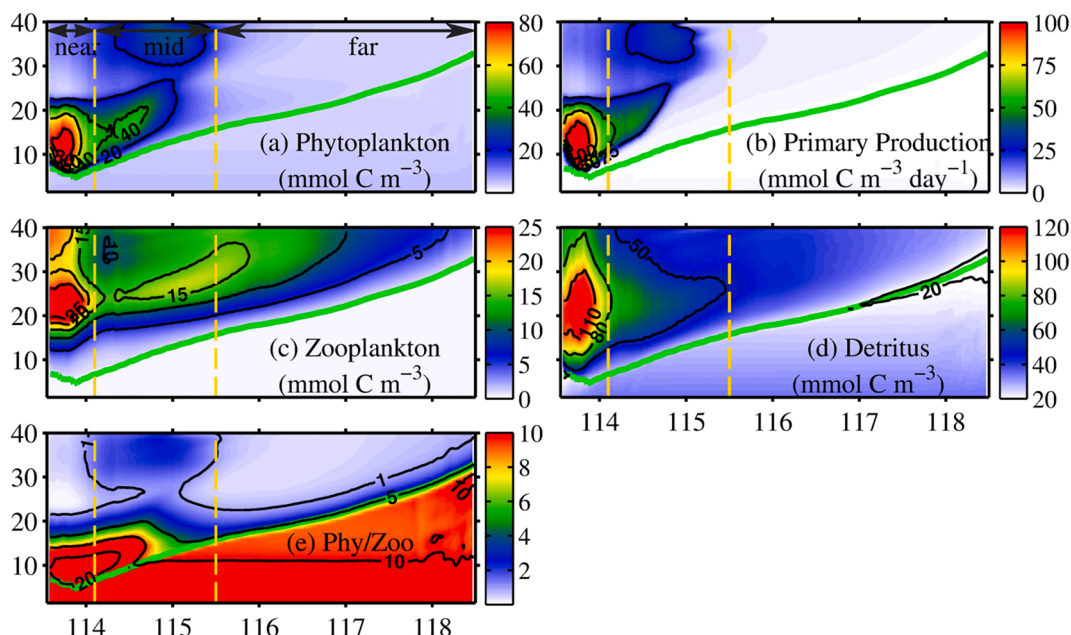
Fig. 7. Time series of along-plume phytoplankton carbon concentration (a), carbon primary production (b), carbon zooplankton concentration (c), detritus carbon concentration (d) and the ratio of phytoplankton to zooplankton (e) in the surface layer as a function of longitude along the plume axis (22.1°N). Green solid lines as in Fig. 6; yellow, vertical dashed lines represent the boundaries of near-field, mid-field and far-field regions. (For interpretation of the references to color in this figure legend, the reader is referred to the web version of this article.)
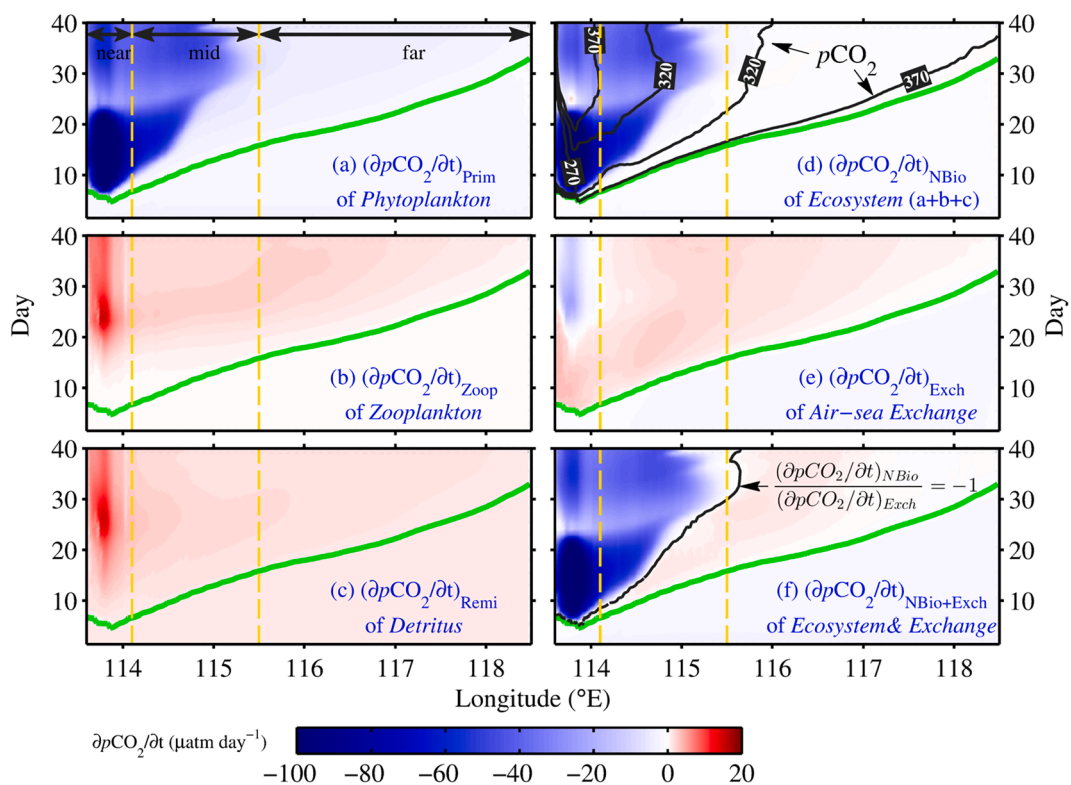

Fig. 8. Time series of along-plume $\partial pCO_2/\partial t$ induced by: (a) phytoplankton primary production, (b) zooplankton metabolism and excretion, (c) remineralization of detritus, (d) net effect of biological processes, (e) air-sea CO_2 exchange, and (f) combined effects of air-sea exchange and biological processes in the surface layer as a function of longitude along the plume axis (22.1°N). Positive (red) and negative (blue) values represent the addition and removal of pCO_2, respectively. Black solid lines in panel (d) indicate the distribution of surface pCO_2, and those in panel (f) indicate the boundary where the magnitude of CO_2 consumption by biological processes equals the CO_2 addition by air-sea exchange. Thus, biological processes exceed the air-sea exchange to the left of the boundary, whereas the air-sea exchange is more important to the right of the boundary. Green solid lines and yellow dashed lines as in Fig. 7. (For interpretation of the references to color in this figure legend, the reader is referred to the web version of this article.)

Table 1
Statistics for different variables in near-, mid- and far-field.

	Near-field		Mid-field	Far-field
	Stage I	Stage II		
Salinity	21.85 ± 5.59 (13.36 to 32.93)	17.62 ± 3.90 (13.26 to 25.03)	29.02 ± 1.49 (25.49 to 32.98)	31.46 ± 0.6 (29.99 to 33.00)
NO_3	15.44 ± 12.16	35.70 ± 11.16	4.33 ± 4.83	0.01 ± 0.01
Phytoplankton	61 ± 20	12 ± 7	22 ± 9	5 ± 2
Zooplankton	8 ± 7	21 ± 6	11 ± 5	9 ± 4
P/Z [†]	18.5 ± 15.3	0.6 ± 0.3	3.4 ± 4.6	0.8 ± 0.8
pCO_2	277 ± 56 (125 to 380)	418 ± 79 (133 to 585)	320 ± 23 (278 to 380)	343 ± 18 (294 to 387)
$(\partial pCO_2/\partial t)_{Prim}$	−85 ± 42 (−158 to −1)	−44 ± 18 (−139 to −10)	−29 ± 20 (−77 to −1)	−3 ± 1 (−12 to −1)
$(\partial pCO_2/\partial t)_{NBio}$	−83 ± 42 (−154 to −0.1)	−33 ± 18 (−131 to 3)	−26 ± 19 (−75 to 0.1)	−0.6 ± 0.6 (−8.5 to 0.6)
$(\partial pCO_2/\partial t)_{Exch}$	2 ± 1 (−1 to 4)	−6 ± 6 (−24 to 3)	2 ± 1 (−0.4 to 2)	0.9 ± 0.6 (−0.6 to 2.2)
$(\partial pCO_2/\partial t)_{NBio+Exch}$	−82 ± 42 (−154 to 2)	−38 ± 19 (−131 to −1)	−25 ± 20 (−73 to 2)	0.3 ± 0.6 (−6 to 3)

*Values in brackets are the range of the corresponding variables.
*Unit of NO_3 is µmol kg^{-1}; unit of phytoplankton and zooplankton are mmol C m^{-3}; unit of $(\partial pCO_2/\partial t)_{Prim}$, $(\partial pCO_2/\partial t)_{NBio}$, $(\partial pCO_2/\partial t)_{Exch}$ and $(\partial pCO_2/\partial t)_{NBio+Exch}$ are µatm pCO_2 day^{-1}.
[†] P/Z represents the ratio between phytoplankton and zooplankton.

5.2.3. Effect of air-sea exchange on sea surface pCO₂

The influence of air-sea exchange on sea surface pCO_2 was also derived following the method introduced in section 5.2.2 (Appendix C). The water depth influenced by the air-sea CO_2 exchange was determined by the wind-induced mixing and referred to as the CO_2 penetration depth. Base on the Eq. (B2.8), the CO_2 penetration depth was averagely 1.7 m day^{-1}.

The $(\partial pCO_2/\partial t)_{Exch}$ was generally greater than zero except for that determined in the near-field after day 25 (Fig. 8e), indicating that air-sea exchange primarily played a role in absorbing atmospheric CO_2 and raising seawater pCO_2, an effect opposite to that of the ecosystem. The boundary where the addition of CO_2 by air-sea exchange counter balanced the consumption of CO_2 by the ecosystem is shown in Fig. 8f by the black solid line annotated by $(\partial pCO_2/\partial t)_{NBio}/(\partial pCO_2/\partial t)_{Exch} = -1$. In the near-field, surface pCO_2 was largely regulated by the ecosystem effect rather than air-sea exchange. In the mid-field, the dominant processes controlling the surface pCO_2 transitioned from air-sea exchange to biological processes at any given location due to the enhanced primary production. In the far-field, the magnitude of $(\partial pCO_2/\partial t)_{Exch}$ was slightly higher than that of the $(\partial pCO_2/\partial t)_{NBio}$, resulting in a net pCO_2 addition rate of 0.3 ± 0.6 µatm pCO_2 day^{-1}.

In summary, the biologically-dominated region where surface pCO_2 was determined by biological processes rather than air-sea exchange included the near-field and the mid-field during later stages, when the phytoplankton biomass production showed an obvious increase. In turn, the region dominated by air-sea exchange, where the influence of air-sea exchange on surface pCO_2 exceeded that of biological processes, was comprised of the far-field and the mid-field during the early stage of arrival of the PRP. In the biologically-dominated region, the pCO_2 consumption rate by biological processes was on average ~10x higher than the air-sea CO_2 exchange rate, in agreement with observations of Dai et al. (2008) that the biological CO_2 consumption rate is 2-6x greater than the air-sea CO_2 exchange rate in a plume-associated bloom close to the PRE (Fig. 9a).

5.2.4. Effect of transport on sea surface pCO₂

In the air-sea exchange-dominated region, the simulated surface pCO_2 (standard run) was lower than atmospheric pCO_2 (Fig. 6e),

whereas the surface pCO_2 that was solely determined by mixing processes (control run) was ~40 µatm greater than the atmospheric pCO_2 (Fig. 6j). This indicated that some processes were responsible for the decrease in pCO_2 and thus the uptake of CO_2 from the atmosphere in the air-sea exchange-dominated region. Given that the combined effect of biological processes and air-sea exchange in this region played a role in the addition rather than removal of pCO_2, the low pCO_2 of surface water should be attributed to transport of low pCO_2 water from other zones rather than being locally induced. Vertical transport of low pCO_2 water can be excluded since DIC, TA and pCO_2 in the subsurface layer were higher than those in the surface layer (Figs. 3 and S3). Thus, horizontal transport upstream from the PRP, including advection and diffusion, were considered to be primarily responsible for the delivery of low pCO_2 water, as evidenced by the near overlap between the spreading boundary of the PRP and the 370 µatm pCO_2 contour (Fig. 6e).

The equilibrium time of air-sea CO_2 exchange in the PRP was evaluated by τ_{CO2} (Eq. (1)), i.e., the time scale for the difference of CO_2 between the atmosphere and seawater to decline to 37% of its initial value (Zeebe and Wolf-Gladrow, 2001).

$$\tau_{CO2} = (d/k) \times (DIC/[CO_2]^{sea})/RF \qquad (1)$$

where d is the depth of the surface mixed layer, k is the gas transfer velocity (from Eq. (B2.8)), RF is the Revelle factor (Revelle and Suess, 1957), and $[CO_2]^{sea}$ is the concentration of CO_2 in seawater.

Based on Eq. (1), τ_{CO2} was estimated to be ~100 days in the PRP by the averaged surface mixed layer depth, temperature, salinity, DIC and pCO_2 as 5.5 m, 29 °C, 32, 1870 µmol kg^{-1}, and 363 µatm, respectively. Thus, the time scale for air-sea CO_2 equilibrium in the PRP was longer than 100 days. In contrast, it took only ~10 days for the PRP currents to move from the PRE to the air-sea exchange-dominated regions, based on a PRP current velocity of ~0.2 m s^{-1} (Gan et al., 2010) and a travel distance of ~200 km from 113.6°E to 115.5°E. Under the effect of air-sea exchange, and after 10 days, the pCO_2 of the PRP increased by merely ~1 and 10 µatm based on an initial pCO_2 of 363 and 270 µatm, respectively. Thus, the mismatch between the prolonged air-sea equilibrium time for pCO_2 and the short transport time for the PRP current (=short residence time) led to the finding that the surface pCO_2 of the PRP remained at a low level when the PRP moved from near- and mid-field to the air-sea exchange-dominated region.

The air-sea equilibrium time of other gases is much shorter than that of CO_2. For instance, the equilibrium time of O_2 in the PRP is only ~3 days. The prolonged air-sea CO_2 equilibrium time, >100 days, is attributed to the buffer capacity of the carbonate system of seawater, i.e., the CO_2 changes in seawater are buffered by other carbonate system species, e.g., bicarbonate and carbonate ions (Zeebe and Wolf-Gladrow, 2001).

5.3. Stage-dependent evolution of sea surface pCO₂ in the PRP

The spatiotemporal dynamics of surface pCO_2 and its controlling mechanisms in the three sub-regions of the PRP is illustrated in Fig. 9. In the near-field, surface pCO_2 was primarily determined by ecosystem effects, namely the strong phytoplankton bloom during the early stage, followed by zooplankton proliferation in the later stage. Air-sea exchange played a minor role herein. Hence, the temporal variation of surface pCO_2 in this near-field region of the plume is substantial. During the phytoplankton bloom stage, the biomass of the phytoplankton was ~20 times as that of the zooplankton (Fig. 7 and Table 1). As a result of the enhanced biological CO_2 uptake, the surface pCO_2, with a value of 277 ± 56 µatm, was much lower than the atmospheric pCO_2. During the subsequent stage, the biomass of zooplankton became as twice as that of the phytoplankton (Fig. 7). The weakening of primary production, high zooplankton abundance and enhanced organic remineralization jointly caused that the net effect of the ecosystem was insufficient to drawdown the surface pCO_2 (418 ± 79 µatm) to a level lower than the atmospheric
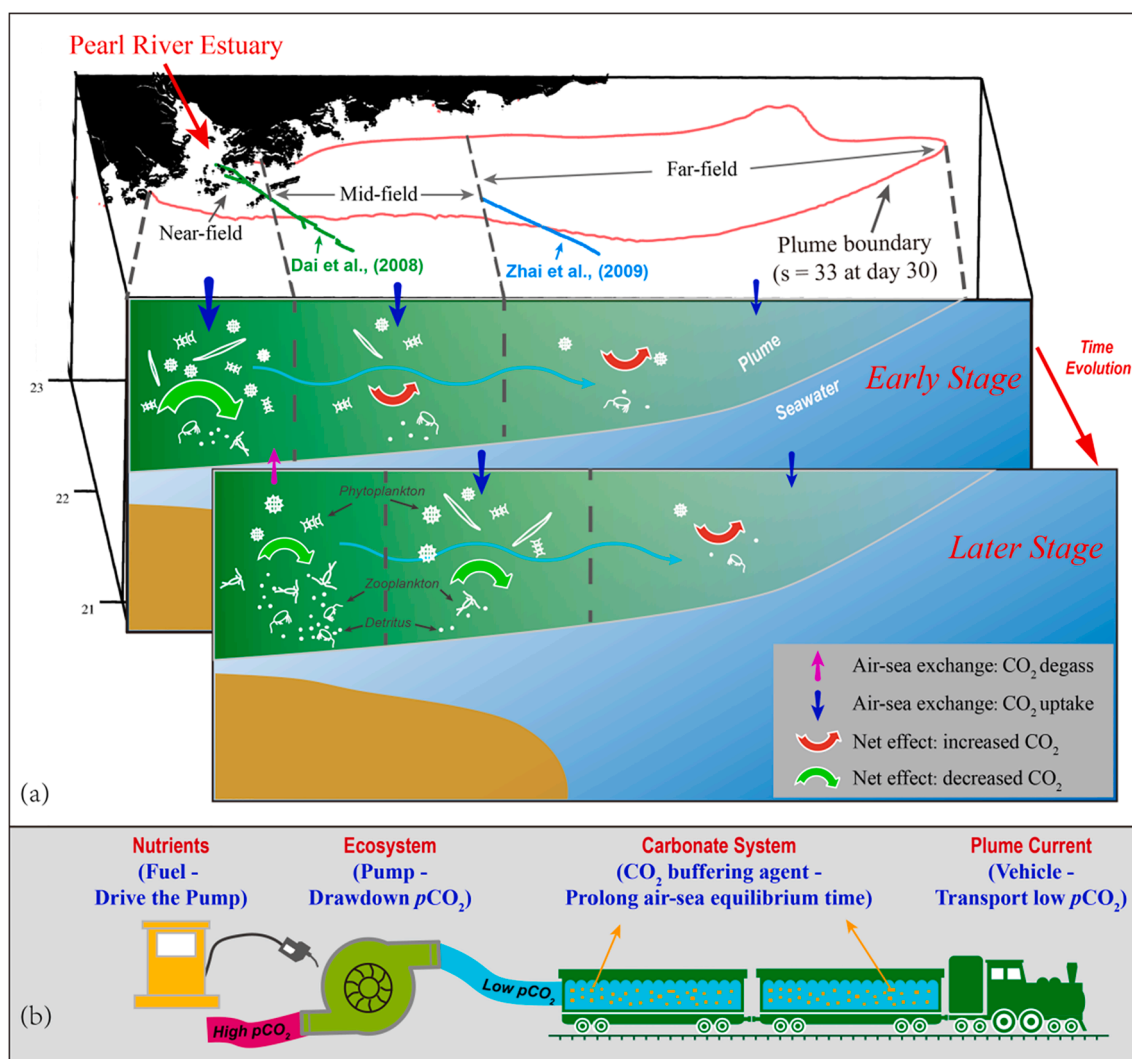
Fig. 9. Schematic diagram showing the controlling mechanisms for surface pCO$_2$ in the Pearl River Plume (PRP): (a) green and turquoise lines in the upper map indicate the sampling stations in the PRP (salinity < 33) by Dai et al. (2008) and Zhai et al. (2009), respectively. Up and down arrows indicate CO$_2$ degassing and CO$_2$ uptake caused by air-sea exchange, respectively. Curved arrows indicate the net effect of biological processes combined with air-sea exchange on pCO$_2$. In the near-field, surface pCO$_2$ is dominated by ecosystem effects characterized by an intense phytoplankton bloom during the early stage of the plume and by enhanced zooplankton activity during the later stage. In the mid-field, the dominant processes controlling surface pCO$_2$ shift from air-sea exchange to biological processes over time. In the far-field, surface pCO$_2$ is dominated by CO$_2$ uptake via air-sea exchange; (b) analogies of the function of nutrients, ecosystem, carbonate system and plume current. (For interpretation of the references to color in this figure legend, the reader is referred to the web version of this article.)

pCO$_2$. Consequently, the near-field region of the PRP evolved over time from an atmospheric CO$_2$ sink to a source when zooplankton attained peak abundance. In the mid-field region, surface pCO$_2$ was dominated by air-sea exchange when the plume water initially arrived at a given location. Subsequently, the biological consumption of pCO$_2$ gradually dominated over the effect of air-sea exchange in association with enhanced primary production, resulting in a net consumption rate of 26 $\pm$ 19 µatm pCO$_2$ day^{-1}. The effect of the biological uptake combined with the delivery of low pCO$_2$ water from the near-field led to the behavior of the mid-field of the PRP as a moderately strong sink for atmospheric CO$_2$, with an average pCO$_2$ of 320 $\pm$ 23 µatm. In the far-field, surface pCO$_2$ was dominated by air-sea exchange and accompanied by a fairly weak ecosystem effect due to nutrient deficiency. The combined effect of biological processes and air-sea exchange caused a pCO$_2$ variation rate < 1 µatm day^{-1}. However, the far-field, with an average pCO$_2$ of 343 $\pm$ 18 µatm, behaved as a weak sink for atmospheric CO$_2$, due to transport of unsaturated pCO$_2$ from the mid-field region and the long air-sea CO$_2$ equilibrium time.

By analogy, the riverine input of nutrients fueled the ecosystem

pump located in the near-field and the mid-field, playing a role in reducing the high pCO$_2$ source from the PRE to levels lower than atmospheric pCO$_2$ (Fig. 9b). Strong plume currents acted as a vehicle for the delivery of low pCO$_2$-waters produced by the ecosystem pump to the continental shelf of the NSCS. The buffer capacity of the carbonate system (as the buffering agent for CO$_2$) slowed down the attainment of air-sea CO$_2$ equilibrium, alleviating the pCO$_2$ increase in the PRP, and consequently allowed the low pCO$_2$ water to travel further away from the estuary and reach the far-afield coastal region.

The conceptual model presented serves to improve our understanding of the controlling mechanisms on the surface pCO$_2$ of the PRP derived from prior studies. For instance, Zhai et al. (2009) suggested that "In the estuarine plume influenced regions, the pCO$_2$-dissolved oxygen (DO) relationship was controlled by the integrated effect of previous community metabolic processes and subsequent air–water exchange". Moreover, Dai et al. (2008) reported a significant phytoplankton bloom associated with fairly low surface pCO$_2$ in the lower reaches of the PRE and the coastal zone of the NSCS. Further understanding for these two researches can be inferred based on the

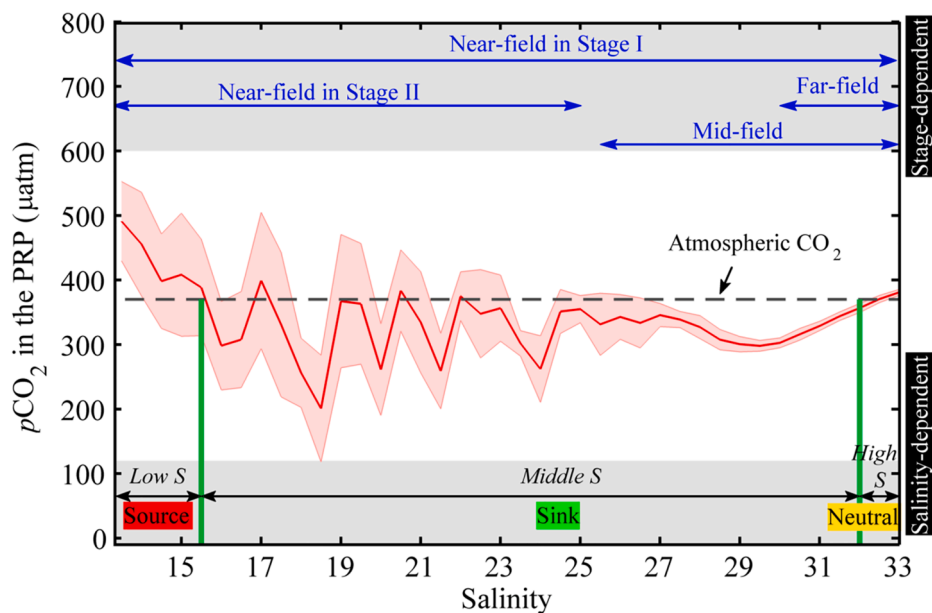**Fig. 10.** Salinity–dependent distribution of pCO_2 in the PRP derived from the data along the plume axis (22.1°N). Red solid line indicates the average pCO_2, and red shading area indicates corresponding standard deviation. (For interpretation of the references to color in this figure legend, the reader is referred to the web version of this article.)

conceptual model. The "estuarine plume influenced regions" in Zhai et al. (2009) refer to the far-field of the PRP, where *in situ* surface pCO_2 is dominated by air-sea exchange owing to low primary production resulted from deficiency of nutrients. The driver for CO_2 uptake in these regions is essentially induced by delivery of low pCO_2 water from the near- and mid-field where intense phytoplankton blooms occur, e.g., the regions (Fig. 9a) reported by Dai et al. (2008).

5.4. Salinity-dependent distribution of sea surface pCO₂ in the PRP

Based on observations alone, it is fairly difficult to deduce the complex spatiotemporal dynamics of surface pCO_2 in river plume, and the salinity-dependent method is generally used to demonstrate the distribution of surface pCO_2 in river plumes (e.g., Huang et al., 2015; Körtzinger, 2003). In the Mississippi River-dominated continental shelf in the northern Gulf of Mexico, Huang et al. (2015) proposed a conceptual model for the distribution of pCO_2 in term of salinity divisions: the low salinity (0–17) subregion is an intensive source of CO_2 to the atmosphere; the middle salinity (17–33) subregion coincides with strong sink of atmospheric CO_2; the high salinity (33–35) subregion shifts from a CO_2 sink to a near neutral status. Such a salinity-dependent distribution of pCO_2 was also exhibited in the PRP based on the model results (Fig. 10). Surface pCO_2 at low salinity (<15.5) was averagely 448 ± 82 µatm, much higher than the atmospheric pCO_2. The intermediate salinity (15.5–32) region behaved as strong CO_2 sink for atmosphere, with an averaged pCO_2 of 329 ± 32 µatm. In the high-salinity end of the PRP (32–33), CO_2 was at equilibrium between the atmosphere and surface seawater (370 ± 9 µatm). Dramatic fluctuations in pCO_2 appeared in the seawater with salinity < 25, i.e., the near-field. The distribution of pCO_2 in the region with salinity of 25–33, including the near-field in stage I, mid-field and far-field, shaped as a downward convex curve, with a minimum pCO_2 of 298 µatm at salinity ~30.

6. Conclusions

A three-dimensional, coupled physical-biogeochemical model was developed in this study to simulate the carbonate system dynamics of the PRP and the NSCS under typical summer conditions. Although idealized, the model successfully captured both the vertical and horizontal

distributions of the carbonate system in the PRP over the NSCS shelf. A quasi-conservative quantitative validation of the model was established. Based on the salinity v.s. TA and DIC relationships, the differences in TA and DIC between the model and observations were < 3.0% and 2.4%, respectively. Using these simulated results, the PRP was divided into three spatially defined sub-regions, including the near-field, mid-field and far-field, based on the dynamics of the carbonate system and surface pCO_2. The relative effects of biological processes and air-sea exchange on surface pCO_2 were established in these regions. Thus, the PRP surface pCO_2 was dominated by biological processes in the near-field and during later stages in the mid-field region associated with high nutrient concentrations and intense biological activity. On the contrary, sea surface pCO_2 in the PRP was dominated by air-sea exchange in the far-field and during early stages in the mid-field region in association with nutrient limitation. It should be noted that CO_2 uptake in the air-sea exchange-dominated region was essentially driven by the phytoplankton blooms in the near- and mid-field. The PRP behaved as an atmospheric CO_2 sink, except in the near-field during the zooplankton proliferation stage. The delivery of low pCO_2 PRP water over the shelf of the NSCS far away from estuary was attributed to the strong plume current associated with the CO_2 buffer capacity of the carbonate system. In term of salinity divisions, the PRP behaved as source, sink and near equilibrium for atmospheric CO_2 in the low, middle and high salinity regions, respectively. Furthermore, CO_2 degassing of the NSCS domain decreased gradually in relation to the decrease in the pCO_2 and increase in the area of the PRP.

In the RiOMar system consisting of the PRP and the NSCS, low pCO_2 water was generated by the enhanced primary production driven by the input of river nutrients. It was maintained in a long period before reaching air-sea equilibrium due to the buffer capacity of the carbonate system, and was transported far away by the strong plume current. The coupled effects of these processes caused spatiotemporal separation between the biological drawdown of seawater pCO_2 and the consequent absorption of atmospheric CO_2.

Declaration of Competing Interest

The authors declare that they have no known competing financial interests or personal relationships that could have appeared to influence

Appendix A. Equations for the biological model

(1) Nitrate concentration ([NO3])

$$\frac{\partial[NO3]}{\partial t} = -\left(\frac{\partial[NO3]}{\partial t}\right)_{PP} + \left(\frac{\partial[NO3]}{\partial t}\right)_{Nitri} \tag{A1.1}$$

$$\left(\frac{\partial[NO3]}{\partial t}\right)_{PP} = \mu_{max} \cdot f(I) \cdot \frac{[NO3]}{(k_{NO3} + [NO3]) \cdot (1 + [NH4]/k_{NH4})} \cdot [P] \tag{A1.2}$$

$$\mu_{max} = \mu_0 \cdot 1.066^T \tag{A1.3}$$

$$f(I) = \frac{\alpha I}{\sqrt{\mu_{max}^2 + \alpha^2 I^2}} \tag{A1.4}$$

$$I(z) = I_0 \cdot PAR_{frac} \cdot exp\left\{-z \cdot \left(k_w + k_{chl} \cdot \int_z^0 Chl(\zeta)d\zeta\right)\right\} \tag{A1.5}$$

$$\begin{cases} I_0 = 450 \cdot sin(t \cdot \pi/16), 0hr \leq t \leq 16hr \text{ for daytime} \\ I_0 = 0, 16hr < t \leq 24hr \text{ for nighttime} \end{cases} \tag{A1.6}$$

$$\left(\frac{\partial[NO3]}{\partial t}\right)_{Nitri} = n_{max}\left(1 - max\left[0, \frac{I - I_{th}}{k_I + I - 2I_{th}}\right]\right) \cdot [NH4] \tag{A1.7}$$

where the *PP* subscript indicates primary production and *Nitri* indicates nitrification; the μ_{max} parameter is the maximum phytoplankton growth rate, $f(I)$ represents the photosynthesis-light (*P-I*) relationship (Evans and Parslow, 1985), K_{NO3} and K_{NH4} are the half-saturation concentrations for NO_3 and NH_4 uptake by phytoplankton, respectively, I is the photosynthetically active radiation (PAR), α is the initial slope of the *P-I* curve, μ_0 is the phytoplankton growth rate, T is temperature, I_0 is the incident light just below the sea surface, it is calculated by the length of daily illumination time t based on Eq. (A1.6), the daily average of I_0 is ~190 W m^{-2} which is close to the observed mean value in the NSCS (Gan et al., 2010), PAR_{frac} is the fraction of light available for photosynthesis, z is the water depth, k_w and k_{chl} are the light attenuation coefficients for seawater and chlorophyll *a*, respectively, n_{max} is the maximum nitrification rate, K_I is the half-saturation light intensity for nitrification inhibition and I_{th} is the threshold for light inhibition of nitrification.

(2) Ammonium concentration ([NH4])

$$\frac{\partial[NH4]}{\partial t} = -\left(\frac{\partial[NH4]}{\partial t}\right)_{PP} - \left(\frac{\partial[NH4]}{\partial t}\right)_{Nitri} + \left(\frac{\partial[NH4]}{\partial t}\right)_{ZM} + \left(\frac{\partial[NH4]}{\partial t}\right)_{ZE} + \left(\frac{\partial[NH4]}{\partial t}\right)_{Re} \tag{A2.1}$$

$$\left(\frac{\partial[NH4]}{\partial t}\right)_{PP} = \mu_{max} \cdot f(I) \cdot \frac{[NH4]}{k_{NH4} + [NH4]} \cdot [P] \tag{A2.2}$$

$$\left(\frac{\partial[NH4]}{\partial t}\right)_{Nitri} = n_{max}\left(1 - max\left[0, \frac{I - I_{th}}{k_I + I - 2I_{th}}\right]\right) \cdot [NH4] \tag{A2.3}$$

$$\left(\frac{\partial[Z]}{\partial t}\right)_{ZE} = L_E \cdot \frac{[P]^2}{k_p + [P]^2} \cdot AE_N \cdot [Z] \tag{A2.4}$$

$$\left(\frac{\partial[Z]}{\partial t}\right)_{ZM} = l_{BM} \cdot [Z] \tag{A2.5}$$

$$\left(\frac{\partial[NH4]}{\partial t}\right)_{Re} = r_{SD} \cdot [SD] + r_{LD} \cdot [LD] \tag{A2.6}$$

where the *ZM* subscript indicates zooplankton excretion due to basal metabolism, *ZE* means zooplankton assimilation-dependent excretion and *Re* represents detritus remineralization; the L_E parameter is the zooplankton excretion-dependent maximum assimilation rate, k_P is the half-saturation concentration for phytoplankton ingestion by zooplankton, AE_N is the zooplankton nitrogen assimilation efficiency, l_{BM} is the zooplankton basal metabolic rate, and r_{SD} and r_{LD} are the remineralization rates for small (<10 μm) and large (≥10 μm) detritus, respectively.

(3) Phytoplankton ([P])

$$\frac{\partial [P]}{\partial t} = \left(\frac{\partial [P]}{\partial t}\right)_{PP} - \left(\frac{\partial [P]}{\partial t}\right)_{ZG} - \left(\frac{\partial [P]}{\partial t}\right)_{MorP} - \left(\frac{\partial [P]}{\partial t}\right)_{AggPhy} - \left(\frac{\partial [P]}{\partial t}\right)_{Sink} \tag{A3.1}$$

$$\left(\frac{\partial [P]}{\partial t}\right)_{PP} = \mu_{max} \cdot f(I) \cdot \left(\frac{[NO3]}{(k_{NO3} + [NO3]) \cdot (1 + [NH4]/k_{NH4})} + \frac{[NH4]}{k_{NH4} + [NH4]}\right) \cdot [P] \tag{A3.2}$$

$$\left(\frac{\partial [P]}{\partial t}\right)_{ZG} = g_{max} \cdot \frac{[P]^2}{k_P + [P]^2} \cdot [Z] \tag{A3.3}$$

$$\left(\frac{\partial [P]}{\partial t}\right)_{MorP} = m_P \cdot [P] \tag{A3.4}$$

$$\left(\frac{\partial [P]}{\partial t}\right)_{AggPhy} = \tau \cdot ([SD] + [P]) \cdot [P] \tag{A3.5}$$

$$\left(\frac{\partial [P]}{\partial t}\right)_{Sink} = w_P \cdot \frac{\partial [P]}{\partial z} \tag{A3.6}$$

where the *ZG* subscript indicates phytoplankton grazing by zooplankton, *MorP* is the phytoplankton mortality, *AggPhy* is the aggregation of phytoplankton, and *Sink* indicates the vertical sinking of phytoplankton; g_{max} is the zooplankton maximum grazing rate, m_P is the phytoplankton mortality rate, τ is the aggregation factor and w_P is the phytoplankton vertical sinking velocity.

(4) Zooplankton ([Z])

$$\frac{\partial [Z]}{\partial t} = \left(\frac{\partial [Z]}{\partial t}\right)_{ZA} - \left(\frac{\partial [Z]}{\partial t}\right)_{ZE} - \left(\frac{\partial [Z]}{\partial t}\right)_{MorZ} - \left(\frac{\partial [Z]}{\partial t}\right)_{ZM} \tag{A4.1}$$

$$\left(\frac{\partial [Z]}{\partial t}\right)_{ZA} = g_{max} \cdot \frac{[P]^2}{k_P + [P]^2} \cdot [Z] \cdot AE_N \tag{A4.2}$$

$$\left(\frac{\partial [Z]}{\partial t}\right)_{ZE} = L_E \cdot \frac{[P]^2}{k_p + [P]^2} \cdot [Z] \cdot AE_N \tag{A4.3}$$

$$\left(\frac{\partial [Z]}{\partial t}\right)_{MorZ} = m_Z \cdot [Z]^2 \tag{A4.4}$$

$$\left(\frac{\partial [Z]}{\partial t}\right)_{ZM} = l_{BM} \cdot [Z] \tag{A4.5}$$

where the *ZA* subscript indicates the assimilation of ingested phytoplankton by zooplankton and *MorZ* indicates the mechanism of zooplankton mortality; the parameter of m_z is the zooplankton mortality rate.

(5) Small detritus ([SD])

$$\frac{\partial [SD]}{\partial t} = \left(\frac{\partial [P]}{\partial t}\right)_{ZP} + \left(\frac{\partial [Z]}{\partial t}\right)_{MorZ} + \left(\frac{\partial [P]}{\partial t}\right)_{MorP} - \left(\frac{\partial [SD]}{\partial t}\right)_{AggSD} - \left(\frac{\partial [SD]}{\partial t}\right)_{Re} - \left(\frac{\partial [SD]}{\partial t}\right)_{Sink} \tag{A5.1}$$

$$\left(\frac{\partial [Z]}{\partial t}\right)_{ZP} = g_{max} \cdot \frac{[P]^2}{k_P + [P]^2} \cdot (1 - AE_N) \cdot [Z] \tag{A5.2}$$

$$\left(\frac{\partial [Z]}{\partial t}\right)_{MorZ} = m_Z \cdot [Z]^2 \tag{A5.3}$$

$$\left(\frac{\partial [P]}{\partial t}\right)_{MorP} = m_P \cdot [P] \tag{A5.4}$$

$$\left(\frac{\partial [SD]}{\partial t}\right)_{AggSD} = \tau \cdot ([SD] + [P]) \cdot [SD] \tag{A5.5}$$

$$\left(\frac{\partial [SD]}{\partial t}\right)_{Re} = r_{SD} \cdot [SD] \tag{A5.6}$$

$$\left(\frac{\partial [SD]}{\partial t}\right)_{Sink} = w_{SD} \cdot \frac{\partial [SD]}{\partial z} \tag{A5.7}$$

where the *ZP* subscript indicates the phytoplankton assimilated by zooplankton and then egested as small detritus, and *AggSD* indicates the aggregation of small detritus; w_{SD} is the vertical sinking velocity of small detritus.

(6) Large Detritus ([LD])

$$\frac{\partial[LD]}{\partial t} = \left(\frac{\partial[LD]}{\partial t}\right)_{AggLD} - \left(\frac{\partial[LD]}{\partial t}\right)_{Re} - \left(\frac{\partial[LD]}{\partial t}\right)_{Sink} \tag{A6.1}$$

$$\left(\frac{\partial[LD]}{\partial t}\right)_{AggLD} = \tau \cdot ([SD] + [P])^2 \tag{A6.2}$$

$$\left(\frac{\partial[LD]}{\partial t}\right)_{Re} = r_{LD} \cdot [LD] \tag{A6.3}$$

$$\left(\frac{\partial[LD]}{\partial t}\right)_{Sink} = w_{LD} \cdot \frac{\partial[LD]}{\partial z} \tag{A6.4}$$

where the *AggLD* subscript indicates the aggregation of large detritus, and w_{LD} is the vertical sinking velocity of large detritus.

Appendix B. Equations for the carbonate system module

(1) Total Alkalinity ([TA])

$$\frac{\partial[TA]}{\partial t} = \left(\frac{\partial[TA]}{\partial t}\right)_{PP} - \left(\frac{\partial[TA]}{\partial t}\right)_{Nitri} \tag{B1.1}$$

$$\left(\frac{\partial[TA]}{\partial t}\right)_{PP} = \frac{\mu_{max} \cdot f(I) \cdot [NO3] \cdot [P]}{(k_{NO3} + [NO3]) \cdot (1 + [NH4]/k_{NH4})} \tag{B1.2}$$

$$\left(\frac{\partial[TA]}{\partial t}\right)_{Nitri} = n_{max} \cdot \left(1 - max\left[0, \frac{I - I_0}{K_I + I - 2 \cdot I_0}\right]\right) \cdot [NH4] \tag{B1.3}$$

where the *PP* subscript indicates the primary production and *Nitri* indicates the nitrification; the parameters in Eqs. (B1.2) and (B1.3) are described in Eqs. (A1.2) and (A1.7), respectively.

(2) Dissolved inorganic carbon concentration ([DIC])

$$\frac{\partial[DIC]}{\partial t} = \left(\frac{\partial[DIC]}{\partial t}\right)_{Bio} + \left(\frac{\partial[DIC]}{\partial t}\right)_{Flux} \tag{B2.1}$$

$$\left(\frac{\partial[DIC]}{\partial t}\right)_{Bio} = -\left(\frac{\partial[DIC]}{\partial t}\right)_{PP} + \left(\frac{\partial[DIC]}{\partial t}\right)_{Zoo} + \left(\frac{\partial[DIC]}{\partial t}\right)_{Re} \tag{B2.2}$$

$$\left(\frac{\partial[DIC]}{\partial t}\right)_{PP} = R_{CN} \cdot \mu_{max} \cdot f(I) \cdot \left(\frac{[NO3]}{(k_{NO3} + [NO3]) \cdot (1 + [NH4]/k_{NH4})} \cdot [P] + \frac{[NH4]}{k_A + [NH4]} \cdot [P]\right) \tag{B2.3}$$

$$\left(\frac{\partial[DIC]}{\partial t}\right)_{Zoo} = R_{CN} \cdot \left(l_{BM} \cdot [Z] + \frac{L_E \cdot [P]^2}{K_P + [P]^2} \cdot AE_N \cdot [Z]\right) \tag{B2.4}$$

$$\left(\frac{\partial[DIC]}{\partial t}\right)_{Re} = r_{SD} \cdot [SD] + r_{LD} \cdot [LD] \tag{B2.5}$$

$$\left(\frac{\partial[DIC]}{\partial t}\right)_{Flux} = \frac{F_{CO2}}{H} \tag{B2.6}$$

$$F_{CO2} = k \cdot K_H \cdot \Delta pCO_2 \tag{B2.7}$$

$$k = 0.31 \cdot u^2 \cdot \left(\frac{S_C}{660}\right)^{-\frac{1}{2}} \tag{B2.8}$$

where the *Bio* subscript represents the biological processes, *PP* indicates the primary production, *Zoo* means the metabolism and excretion rates of zooplankton, *Re* is the remineralization, and *Flux* indicates the air-sea CO_2 exchange; R_{CN} is the ratio of carbon to nitrogen of the phytoplankton and zooplankton, the parameters in Eq. (B2.3) are described in Eqs. (A1.2) and (A2.2), those in Eq. (B2.4) are described in Eqs. (A2.4) and (A2.5), r_{SD} and r_{LD} are the remineralization rates of small and large detritus, respectively, F_{CO2} is the air-sea CO_2 flux, H is the water depth that is influenced by air-sea exchanges, k is the CO_2 gas transfer velocity, K_H is the solubility coefficient of CO_2 in seawater (Weiss, 1974), ΔpCO_2 is the difference in pCO_2 between the surface water and atmosphere, u is the wind speed at 10 m above the sea surface and S_C is the Schmidt number for CO_2 (Wanninkhof, 1992).

(3) pCO_2 ($[pCO_2]$)

Seawater pCO_2 is calculated based on the equilibrium of the carbonate system (Zeebe and Wolf-Gladrow, 2001).

$$\frac{\partial [pCO_2]}{\partial t} = f\left(\frac{\partial [DIC]}{\partial t}, \frac{\partial [TA]}{\partial t}, \frac{\partial [T]}{\partial t}, \frac{\partial [S]}{\partial t}\right) \tag{B3.1}$$

where T is the seawater temperature and S is the salinity of seawater.

Appendix C. Method for quantification of individual processes affecting sea surface pCO_2

To quantify the effects of biological processes and air-sea exchange on surface pCO_2, we first derived the corresponding DIC and TA variation (Step 1), and then computed the corresponding changes in pCO_2 (Step 2) based on the model's governing equations (Appendix A and B).

Step 1. Effects on DIC and TA

Variation in DIC ($\partial DIC/\partial t$) caused by the biological terms, including phytoplankton primary production (($\partial DIC/\partial t)_{PP}$), zooplankton metabolism and excretion (($\partial DIC/\partial t)_{Zoo}$) and remineralization of detritus (($\partial DIC/\partial t)_{Re}$) are shown in Eqs. (B2.3), (B2.4) and (B2.5), respectively. The summation of ($\partial DIC/\partial t)_{PP}$, ($\partial DIC/\partial t)_{Re}$ and ($\partial DIC/\partial t)_{Zoo}$ (Eq. (B2.2)) was defined as the net effect of the ecosystem on DIC, i.e., ($\partial DIC/\partial t)_{NetB}$. The effects of primary production and nitrification on TA ($\partial TA/\partial t$) were calculated from Eqs. (B1.2) and (B1.3), respectively.

The influence of air-sea exchanges on DIC (($\partial DIC/\partial t)_{Flux}$) was based on Eq. (B2.6) where the variable of H indicated the water depth influenced by air-sea CO_2 exchanges. Here, H is determined by the wind-induced mixing and referred to as the CO_2 penetration depth. The equation for H is $H = k \cdot t$, where k (cm h^{-1}) is the CO_2 gas transfer velocity in Eq. (B2.8) (Wanninkhof, 1992), t is the time which equals to one day here. In typical summer conditions, H ranges from 1.5 to 1.8 m day^{-1} with an average value of 1.7 m day^{-1}.

Step 2. Effects on pCO_2

Seawater CO_2 is determined by the equilibrium of carbonate species rather than CO_2 mass conservation. Thus, the variation in pCO_2 ($\partial pCO_2/\partial t$) caused by biological processes and air-sea exchange should be quantified based on the corresponding variation in TA ($\partial TA/\partial t$) and DIC ($\partial DIC/\partial t$). The $\partial pCO_2/\partial t$ at a given location from time t_1 to t_2 was evaluated as follows: (1) pCO_2 at the initial time t_1 (pCO_2^{t1}) was quantified by the initial DIC (DIC^{t1}) and TA (TA^{t1}) using the CO2SYS program (Lewis and Wallace, 1998); (2) $\partial DIC/\partial t$ and $\partial TA/\partial t$ caused by different processes were evaluated following Step 1; (3) the corresponding DIC and TA at t_2 were equal to $DIC^{t1} + \Delta t \cdot \partial DIC/\partial t$ and $TA^{t1} + \Delta t \cdot \partial TA/\partial t$, respectively; (4) the pCO_2 at t_2 (pCO_2^{t2}) under the influence of a given process was calculated by the corresponding DIC^{t2} and TA^{t2}; (5) the difference between pCO_2^{t2} and pCO_2^{t1} was defined as the effects of the corresponding process on pCO_2 during the time interval Δt, with a negative or positive value indicating the removal or addition of pCO_2, respectively.

Appendix D

See Table D1.

Table D1
Ecosystem and carbonate system model parameters.

Description	Symbol	Value	Unit
Half-saturation concentration for NO$_3$ uptake	K_{NO3}	0.5	mmol N m^{-3}
Half-saturation concentration for NH$_4$ uptake	K_{NH4}	0.5	mmol N m^{-3}
Initial slope of the *P-I* curve	α	0.025	mgC (mg Chl W m^{-2} d)$^{-1}$
Phytoplankton growth rate	μ_0	0.59	d^{-1}
Fraction of light available for photosynthesis	PAR_{frac}	0.43	
Light attenuation coefficient for seawater	k_w	0.04	m^{-1}
Light attenuation coefficient for chlorophyll *a*	k_{chl}	0.025	(mg Chl)$^{-1}$ m^{-2}
Maximum nitrification rate	n_{max}	0.05	d^{-1}
Half-saturation light intensity for nitrification inhibition	K_I	0.1	W m^{-2}
Threshold for light-inhibition of nitrification	I_{th}	0.0095	W m^{-2}
Maximum rate of assimilation-related zooplankton excretion	L_E	0.1	d^{-1}
Half-saturation concentration for phytoplankton ingestion by zooplankton	k_P	1	(mmol N m^{-3})^2
Zooplankton assimilation efficiency for nitrogen	AE_N	0.75	
Zooplankton basal metabolism rate	l_{BM}	0.1	d^{-1}
Small detritus remineralization rate	r_{SD}	0.03	d^{-1}
Large detritus remineralization rate	r_{LD}	0.01	d^{-1}
Zooplankton maximum grazing rate	g_{max}	0.6	(mmol N m^{-3})$^{-1}$ d^{-1}
Phytoplankton mortality rate	m_P	0.15	d^{-1}
Aggregation factor	τ	0.005	(mmol N m^{-3})$^{-1}$ d^{-1}
Sinking velocity of phytoplankton	w_P	0.1	m d^{-1}
Zooplankton mortality rate	m_Z	0.025	(mmol N m^{-3})$^{-1}$ d^{-1}
Sinking velocity for small detritus	w_{SD}	0.1	m d^{-1}
Sinking velocity for large detritus	w_{LD}	1	m d^{-1}
Carbon to nitrogen ratio for phytoplankton and zooplankton	R_{CN}	6.625	mol C (mol N)$^{-1}$

Appendix E. Supplementary material

Supplementary data to this article can be found online at https://doi.org/10.1016/j.pocean.2020.102457.

References

Bauer, J.E., Cai, W.J., Raymond, P.A., Bianchi, T.S., Hopkinson, C.S., Regnier, P.A.G., 2013. The changing carbon cycle of the coastal ocean. Nature 504 (7478), 61–70.

Borges, A.V., Delille, B., Frankignoulle, M., 2005. Budgeting sinks and sources of CO_2 in the coastal ocean: diversity of ecosystems counts. Geophys. Res. Lett. 32 (14), L14601. https://doi.org/10.1029/2005GL023053.

Cai, W.J., 2011. Estuarine and coastal ocean carbon paradox: CO_2 sinks or sites of terrestrial carbon incineration? Ann. Rev. Mar. Sci. 3 (1), 123–145.

Cao, Z.M., Dai, M.H., Zheng, N., Wang, D.L., Li, Q., Zhai, W.D., Meng, F.F., Gan, J.P., 2011. Dynamics of the carbonate system in a large continental shelf system under the influence of both a river plume and coastal upwelling. J. Geophys. Res. 116, G02010. https://doi.org/10.1029/2010JG001596.

Cao, Z.M., Yang, W., Zhao, Y.Y., Guo, X.H., Yin, Z.Q., Du, C.J., Zhao, H.D., Dai, M.H., 2020. Diagnosis of CO_2 dynamics and fluxes in global coastal oceans. Natl. Sci. Rev. 7, 786–797. https://doi.org/10.1093/nsr/nwz105.

Chao, S.Y., 1988. Wind-driven motion of estuarine plumes. J. Phys. Oceanogr. 18 (8), 1144–1166.

Chen, C.A., Borges, A.V., 2009. Reconciling opposing views on carbon cycling in the coastal ocean: continental shelves as sinks and near-shore ecosystems as sources of atmospheric CO_2. Deep Sea Res. II 56 (8–10), 578–590.

Chen, C.A., Huang, T.H., Fu, Y.H., Bai, Y., He, X.Q., 2012. Strong sources of CO_2 in upper estuaries become sinks of CO_2 in large river plumes. Curr. Opin. Environ. Sustain. 4 (2), 179–185.

Chen, C.T.A., Huang, T.H., Chen, Y.C., Bai, Y., He, X.Q., Kang, Y., 2013. Air-sea exchanges of CO_2 in the world's coastal seas. Biogeosciences 10 (10), 6509–6544. https://doi.org/10.5194/bg-10-6509-2013.

Chou, W.C., Gong, G.C., Sheu, D.D., Jan, S., Hung, C.C., Chen, C.C., 2009. Reconciling the paradox that the heterotrophic waters of the East China Sea shelf act as a significant CO_2 sink during the summertime: evidence and implications. Geophys. Res. Lett. 36 (15), L15607. https://doi.org/10.1029/2009GL038475.

Cooley, S.R., Coles, V.J., Subramaniam, A., Yager, P.L., 2007. Seasonal variations in the Amazon plume-related atmospheric carbon sink. Global Biogeochem. Cycles 21 (3), GB3014. https://doi.org/10.1029/2006GB002831.

Dagg, M., Benner, R., Lohrenz, S., Lawrence, D., 2004. Transformation of dissolved and particulate materials on continental shelves influenced by large rivers: plume processes. Cont. Shelf Res. 24 (7–8), 833–858.

Dai, A.G., 2016. Historical and future changes in streamflow and continental runoff. In: Q. Tang and T. Oki, Terrestrial water cycle and climate change: Natural and human-induced impacts, pp. 17–37.

Dai, M.H., Cao, Z.M., Guo, X.H., Zhai, W.D., Liu, Z.Y., Yin, Z.Q., Xu, Y.P., Gan, J.P., Hu, J.Y., Du, C.J., 2013. Why are some marginal seas sources of atmospheric CO_2? Geophys. Res. Lett. 40 (10), 2154–2158. https://doi.org/10.1002/grl.50390.

Dai, M.H., Gan, J.P., Han, A.Q., Kung, H.S., Yin, Z.Q., 2014. Physical dynamics and biogeochemistry of the Pearl River plume, in Biogeochemical Dynamics at Major River-Coastal Interfaces: Linkages with Global Change, Bianchi T., Allison M., and Cai W.-J., Editors, Cambridge University Press, 321-352.

Dai, M.H., Zhai, W.D., Cai, W.J., Callahan, J., Huang, B.W., Shang, S.L., Huang, T., Li, X., Lu, Z.M., Chen, W.F., Chen, Z.Z., 2008. Effects of an estuarine plume-associated bloom on the carbonate system in the lower reaches of the Pearl River estuary and the coastal zone of the northern South China Sea. Cont. Shelf Res. 28 (12), 1416–1423.

de la Paz, M., Padín, X.A., Ríos, A.F., Pérez, F.F., 2010. Surface fCO_2 variability in the Loire plume and adjacent shelf waters: high spatio-temporal resolution study using ships of opportunity. Mar. Chem. 118 (3–4), 108–118.

Evans, G.T., Parslow, J.S., 1985. A model of annual plankton cycles. Biol. Oceanography 3 (3), 327–347.

Fasham, M.J.R., Ducklow, H.W., McKelvie, S.M., 1990. A nitrogen-based model of plankton dynamics in the oceanic mixed layer. J. Mar. Res. 48 (3), 591–639.

Fennel, K., Wilkin, J., Levin, J., Moisan, J., O'Reilly, J., Haidvogel, D., 2006. Nitrogen cycling in the Middle Atlantic Bight: results from a three-dimensional model and implications for the North Atlantic nitrogen budget. Global Biogeochem. Cycles 20 (3), GB3007. https://doi.org/10.1029/2005GB002456.

Fennel, K., Wilkin, J., Previdi, M., Najjar, R., 2008. Denitrification effects on air-sea CO_2 flux in the coastal ocean: Simulations for the northwest North Atlantic. Geophys. Res. Lett. 35 (24), L24608. https://doi.org/10.1029/2008GL036147.

Fong, D.A., Geyer, W.R., 2002. The alongshore transport of freshwater in a surface-trapped river plume. J. Phys. Oceanogr. 32 (3), 957–972.

Gan, J.P., Allen, J.S., 2005. On open boundary conditions for a limited-area coastal model off Oregon. Part 1: response to idealized wind forcing. Ocean Model. 8 (1), 115–133.

Gan, J.P., Li, L., Wang, D.X., Guo, X.H., 2009a. Interaction of a river plume with coastal upwelling in the northeastern South China Sea. Cont. Shelf Res. 29 (4), 728–740.

Gan, J.P., Cheung, A.Y.Y., Guo, X.H., Li, L., 2009b. Intensified upwelling over a widened shelf in the northeastern South China Sea. J. Geophys. Res. 114, C09019. https://doi.org/10.1029/2007JC004660.

Gan, J.P., Lu, Z.M., Dai, M.H., Cheung, A.Y.Y., Liu, H.B., Harrison, P., 2010. Biological response to intensified upwelling and to a river plume in the northeastern South

China Sea: a modeling study. J. Geophys. Res. 115, C09001. https://doi.org/10.1029/2009JC005569.

Guo, X.H., Cai, W.J., Zhai, W.D., Dai, M.H., Wang, Y., Chen, B.S., 2008. Seasonal variations in the inorganic carbon system in the Pearl River (Zhujiang) estuary. Cont. Shelf Res. 28 (12), 1424–1434.

Guo, X.H., Zhai, W.D., Dai, M.H., Zhang, C., Bai, Y., Xu, Y., Li, Q., Wang, G.Z., 2015. Air-sea CO_2 fluxes in the East China Sea based on multiple-year underway observations. Biogeosciences, 12(18): 5495-5514, doi: 10.5194/bg-12-5495-2015, 2015.

Han, A.Q., Dai, M.H., Kao, S.J., Gan, J.P., Li, Q., Wang, L.F., Zhai, W.D., Wang, L., 2012. Nutrient dynamics and biological consumption in a large continental shelf system under the influence of both a river plume and coastal upwelling. Limnol. Oceanogr. 57 (2), 486–502.

Hetland, R.D., 2005. Relating river plume structure to vertical mixing. J. Phys. Oceanogr. 35 (9), 1667–1688.

Hickey, B.M., Kudela, R.M., Nash, J.D., Bruland, K.W., Peterson, W.T., MacCready, P., Lessard, E.J., Jay, D.A., Banas, N.S., Baptista, A.M., Dever, E.P., Kosro, P.M., Kilcher, L.K., Horner-Devine, A.R., Zaron, E.D., McCabe, R.M., Peterson, J.O., Orton, P.M., Pan, J., Lohan, M.C., 2010. River influences on shelf ecosystems: introduction and synthesis. J. Geophys. Res. 115, C00B17. https://doi.org/10.1029/2009JC005452.

Hofmann, E., Druon, J., Fennel, K., Friedrichs, M., Haidvogel, D., Lee, C., Mannino, A., McClain, C., Najjar, R., O'Reilly, J., 2008. Eastern US continental shelf carbon budget integrating models, data assimilation, and analysis. Oceanography 21 (1), 86–104.

Horner-Devine, A.R., Hetland, R.D., MacDonald, D.G., 2015. Mixing and transport in coastal river plumes. Annu. Rev. Fluid Mech. 47 (1), 569–594.

Huang, W.J., Cai, W.J., Wang, Y.C., Lohrenz, S.E., Murrell, M.C., 2015. The carbon dioxide system on the Mississippi River-dominated continental shelf in the northern Gulf of Mexico: 1. distribution and air-sea CO_2 flux. J. Geophys. Res. 120 (3), 1429–1445. https://doi.org/10.1002/2014JC010498.

Ibánhez, J.S.P., Araujo, M., Lefèvre, N., 2016. The overlooked tropical oceanic CO_2 sink. Geophys. Res. Lett. 43 (8), 3804–3812. https://doi.org/10.1002/2016GL068020.

Ibánhez, J.S.P., Diverrès, D., Araujo, M., Lefèvre, N., 2015. Seasonal and interannual variability of sea-air CO_2 fluxes in the tropical Atlantic affected by the Amazon River plume. Global Biogeochem. Cycles 29 (10), 1640–1655. https://doi.org/10.1002/2015GB005110.

Ketchum, B.H., 1983. Estuarine characteristics, Estuaries and enclosed seas. Ecosystems of the World. Elsevier, Amsterdam, pp. 1–14.

Körtzinger, A., 2003. A significant CO_2 sink in the tropical Atlantic Ocean associated with the Amazon River plume. Geophys. Res. Lett. 30 (24), 2287. https://doi.org/10.1029/2003GL018841.

Laruelle, G.G., Lauerwald, R., Pfeil, B., Regnier, P., 2014. Regionalized global budget of the CO_2 exchange at the air-water interface in continental shelf seas. Global Biogeochem. Cycles 28 (11), 1199–1214. https://doi.org/10.1002/2014GB004832.

Lewis, E., Wallace, D., 1998. Program developed for CO_2 system calculations. ORNL/CDIAC-105, Carbon Dioxide Information Analysis Center. Oak Ridge National Laboratory, U.S. Department of Energy, Oak Ridge, Tennessee.

Mellor, G.L., Yamada, T., 1982. Development of a turbulence closure model for geophysical fluid problems. Rev. Geophys. Space Phys. 20 (4), 851–875.

Molleri, G.S.F., Novo, E.M.L.D., Kampel, M., 2010. Space-time variability of the Amazon River plume based on satellite ocean color. Cont. Shelf Res. 30 (3–4), 342–352.

Ou, S.Y., Zhang, H., Wang, D.X., 2009. Dynamics of the buoyant plume off the Pearl River Estuary in summer. Environ. Fluid Mech. 9 (5), 471–492.

Revelle, R., Suess, H.E., 1957. Carbon dioxide exchange between atmosphere and ocean and the question of an increase of atmospheric CO_2 during the past decades. Tellus 9 (1), 18–27.

Shchepetkin, A.F., McWilliams, J.C., 2005. The regional oceanic modeling system (ROMS): a split-explicit, free-surface, topography-following-coordinate oceanic model. Ocean Model. 9 (4), 347–404.

Song, Y.H., Haidvogel, D., 1994. A semi-implicit ocean circulation model using a generalized topography-following coordinate system. J. Comput. Phys. 115 (1), 228–244.

Spitz, Y.H., Allen, J.S., Gan, J.P., 2005. Modeling of ecosystem processes on the Oregon shelf during the 2001 summer upwelling. J. Geophys. Res. 110, C10S17. https://doi.org/10.1029/2005JC002870.

Su, J.Z., Dai, M.H., He, B.Y., Wang, L., Gan, J.P., Guo, X.H., Zhao, H.D., Yu, F.L., 2017. Tracing the origin of the oxygen-consuming organic matter in the hypoxic zone in a large eutrophic estuary: the lower reach of the Pearl River Estuary, China. Biogeosciences 14 (18), 4085–4099. https://doi.org/10.5194/bg-14-4085-2017.

Ternon, J.F., Oudot, C., Dessier, A., Diverres, D., 2000. A seasonal tropical sink for atmospheric CO_2 in the Atlantic ocean: the role of the Amazon River discharge. Mar. Chem. 68 (3), 183–201.

Tseng, C., Liu, K.K., Gong, G.C., Shen, P.Y., Cai, W.J., 2011. CO_2 uptake in the East China Sea relying on Changjiang runoff is prone to change. Geophys. Res. Lett. 38 (24), L24609. https://doi.org/10.1029/2011GL049774.

Walker, N.D., Wiseman, W.J., Rouse, L.J., Babin, A., 2005. Effects of river discharge, wind stress, and slope eddies on circulation and the satellite-observed structure of the Mississippi River Plume. J. Coastal Res. 21 (6), 1228–1244.

Wanninkhof, R., 1992. Relationship between wind speed and gas exchange over the ocean. J. Geophys. Res. 97 (C5), 7373–7382. https://doi.org/10.1029/92JC00188.

Weiss, R.F., 1974. Carbon dioxide in water and seawater: the solubility of a non-ideal gas. Mar. Chem. 2 (3), 203–215.

Zeebe, R.E., Wolf-Gladrow, D., 2001. CO_2 in seawater: equilibrium, kinetics, isotopes. In: Oceanography series, 65. Elsevier Science, Amsterdam, pp. 346–pp.

Zhai, W.D., Dai, M.H., Cai, W.J., 2009. Coupling of surface pCO_2 and dissolved oxygen in the northern South China Sea: impacts of contrasting coastal processes. Biogeosciences 6 (11), 2589–2598. https://doi.org/10.5194/bg-6-2589-2009.

Zhai, W.D., Dai, M.H., Chen, B.S., Guo, X.H., Li, Q., Shang, S.L., Zhang, C.Y., Cai, W.J., Wang, D.X., 2013. Seasonal variations of sea-air CO_2 fluxes in the largest tropical marginal sea (South China Sea) based on multiple-year underway measurements. Biogeosciences 10 (11), 7775–7791. https://doi.org/10.5194/bg-10-7775-2013.

Zhao, H.D., Kao, S.J., Zhai, W.D., Zang, K.P., Zheng, N., Xu, X.M., Huo, C., Wang, J.Y., 2017. Effects of stratification, organic matter remineralization and bathymetry on summertime oxygen distribution in the Bohai Sea, China. Cont. Shelf Res. 134, 15–25.